

Point-by-point response to the referees ' comments

We thank the two referees for their pertinent comments which certainly helped to improve the manuscript. The referees have brought up some important points and we appreciate the opportunity to address them based on a point-by-point response to their comments, which follows below (in black the original comments from the referees and in red our responses).

Referee # 1

First results are presented for a case study, which look very promising. Overall, it is a very impressive effort. The paper is well written and clearly structured. The English is very good. In my opinion, this paper deserves publication in ACP. I only have minor modifications to suggest.

We are very pleased for the enthusiastic words expressed by the referee. We also appreciate the possibility for further improve the manuscript based on his/her precious suggestions.

Minor comments. The potential for BASIL to measure profiles of moments of turbulent fluctuations in the PBL is of great interest to the community. In the paper, only a short sample of the dataset acquired during HOPE (2 hours) under "ideal" meteorological conditions is presented. I am convinced that such data acquired in more complex situations would be extremely worthy, and that obtaining from an instrument such as BASIL the diurnal evolution of profiles of higher-order moments of turbulent fluctuations would be invaluable for understanding PBL processes associated with night-day transitions, PBL development under cloudy situations and model validation.

We agree with the referee about the enormous value and potential scientific impact of having measurements of the diurnal evolution of higher-order moments of turbulent fluctuations in clear sky conditions, as well as in more complex meteorological situations. For this motivation, after the publication of the present manuscript aimed to demonstrate the capability of our Raman lidar to characterize turbulent processes within the convective boundary layer, we plan to possibly extend the analysis to a variety of clear-sky and cloud-topped convective boundary layer conditions from different field deployments and include these additional results in a forthcoming paper.

At the end of the paper, the authors provide some leads concerning future studies to be undertaken with the BASIL dataset along these lines. I think it would be worthwhile discussing in the paper (maybe in the final section, 1 short paragraph) to what extend the temporal resolution of the flux profiles retrievals could be reduced to hourly (or less) temporal resolutions and if a realistic diurnal evolution of these variables can be extracted from the impressive HOPE dataset.

We agree with the referee about the opportunity to discuss in the paper the feasibility of measurements of turbulent processes with increased temporal resolution which can be obtained by reducing the time window for the application of the auto-covariance approach from two hours to one hour or less, possibly allowing to follow the diurnal evolution of the convective boundary layer. So far attention has been focused only on those time segments characterized by a well-mixed and quasi-stationary convective boundary layer, characterized by a stable or almost stable boundary layer height, which corresponds to the period of its maximum development around local noon. In this regard, it is to be noticed that the selection of a shorted time interval (one hour or less) with respect to the one presently considered (two hours) would lead to an increase of the sampling error, i.e. the error incurred when the statistical characteristics of a measured population are estimated from a subset of the real population (the smaller is the sub-set, the larger is the sampling error). In the future this can be overcome by averaging turbulence profiles measured under similar meteorological conditions. This requires continuous measurements during field campaigns and even more the application of our methodology to data acquired by operational lidar systems such as those present at the ARM Southern Great Plains (SGP) site in Oklahoma (USA), at DWD in Lindenberg

(Germany), and at Meteo-Swiss in Payerne (Switzerland). An example for a pioneering campaign applying these techniques is the Land-Atmosphere Feedback Experiment (LAFE) to be performed in August 2017 at the SGP site (see www.arm.gov/publications/programdocs/doi-sc-arm-16-038.pdf).

Additionally, the selection of a well-mixed and quasi-stationary convective boundary layer characterized by a stable height allows for the use of a simple data de-trending approach based on the application of a linear fit to the atmospheric variable time series and the following removal of the mean value. This approach cannot be applied in the presence of high-frequency variations associated with synoptically induced transients such as frontal passages or dry-lines. However, we believe that a modified version of this de-trending approach will be effectively applicable to also remove influences associated with large-scale advection, synoptic processes, and, ultimately, the diurnal cycle and the presence of a cloud-topped convective boundary layer.

All these aspects are now clearly discussed in the final section of the paper, where the following paragraph has been introduced: “As a final remark, we need to specify that we foresee the possibility to apply this approach to characterize the diurnal evolution of turbulent processes within the convective boundary layer, by monitoring the changing patterns of water vapour and temperature higher-order moments during its different evolution phases, including day-to-night and night-to-day transitions, possibly with increased temporal resolution. However, measurements of turbulent processes with increased temporal resolution obtained by reducing the time window for the application of the auto-covariance approach to one hour or less would lead to an increase of the sampling error. This can be overcome by the analysis of continuous measurements such as those carried out at observatories like the ARM Southern Great Plains (SGP) site in Oklahoma (USA), the DWD Meteorologisches Observatorium in Lindenberg (Germany) and the Meteo-Swiss Centre for Meteorological Measurement Technology in Payerne (Switzerland). Furthermore, more data will become available via new field campaigns. An example for a pioneering campaign applying these techniques is the forthcoming Land-Atmosphere Feedback Experiment (LAFE, Wulfmeyer and Turner, 2016) to be held at the SGP site (see www.arm.gov/publications/programdocs/doi-sc-arm-16-038.pdf). Finally, in order to apply the auto-covariance approach to characterize the diurnal evolution of turbulent processes in clear sky conditions, as well as in more complex meteorological situations, i.e. in the presence of large-scale advection, synoptic processes and cloud-topped convective boundary layer, modifications in the de-trending approach considered in the present paper are required.”

P6, l21: I am aware that moisture profiles can be extracted from GPS tomography. Can this also be done for temperature? Or is it just a cut/paste from the water vapour paragraph above?

Temperature profiles cannot be extracted from GPS tomography in the lower troposphere and reference to this capability was only an oversight. The corresponding sentence has been corrected and now reads: “These two calibration constants can be determined through the comparison of the lidar signal ratio with simultaneous and co-located temperature measurements from different sensors (e.g., from radiosondes, microwave radiometers, etc.)”.

P17, l26: “starting”

Corrected. Now the sentence reads: “... with cirrus clouds starting from 15 UTC”.

P18, l18: “aerosols property”

Corrected. Now the sentence reads: “... by exploiting aerosols property to act as atmospheric tracers”.

P19, l24-25: “[: : :] as in fact: : : column.” This sentence is unclear, please rephrase.

The sentence has been rephrased as follows: “This property makes lidar systems much more suitable for studying turbulence statistics than in-situ sounding systems. In fact, because of the capability of the formers to monitor the vertical air column above the station as opposed to radiosondes, undergoing a horizontal drift during their ascent and consequently a deviation from the vertical, lidar systems guarantee the capability to measure turbulence statistics within the turbulent eddies involved in the boundary layer mixing processes.”

Figure 9: it is a bit odd to see that a large part of the signal is off-scale on this figure. Why is it so? This should be improved.

We improved figure 9 by changing the full-scale value from 250 to 800 s and now values in the lower portion of the CBL are within the scale. The text describing the figure has also been slightly changed as follows: “The integral time scale of both water vapour mixing ratio and temperature fluctuations is found to have large values (also in excess of 200 s, up to 500 s for water vapour) in the lower portion of the CBL up to @ 750 m (i.e. $z/z_i < 0.6$).”

Figure 13: same comment as above, especially for Fig. 13b.

We improved figure 13 by changing the full-scale values both in panel a and b. Full-scale values are now -15/+15 for panel a and -5/+25 for panel b.

Referee # 2

In the abstract is missing a sort of "punch line". Why the measured values in terms of water vapor and temperature are important and who is going to use those measurements?

We agree with the referee that a clear statement of the relevance and potential impact of these measurements, already present in the introduction, should also appear in the abstract. For this purpose, the following sentence was introduced in the abstract: “These measurements, in combination with measurements from other lidar and in-situ systems, are important to verify and possibly improve turbulence and convection parameterization in weather and climate models at different scales down to the grey zone (grid increment ~ 1 km) (Wulfmeyer et al. 2016)”.

The retrieved planetary boundary layer height in the manuscript is 1290+/-77. I know that this number comes from the standard deviation calculation, but which is the physical meaning of this value as the lidar resolution is discrete? Doesn't make more physical sense to round up to the closest available range bin?

The approach used in the present research effort to estimate the planetary boundary layer height is based on the detection of the strongest gradient in the particle backscatter coefficient at 1064 nm. The signal strength of the elastic signal at 1064 nm is much larger than the strength of the vibrational and rotational Raman signals, which have used to determine water vapour mixing ratio and temperature profiles. As a result of this larger strength, the elastic signal at 1064 nm is acquired with a much higher vertical resolution (7.5 m) than the one considered for the water vapour and temperature measurements, i.e. 90 m and 30 m, respectively.

The standard deviation of ± 77 m associated to the mean boundary layer height (1290 m) is aimed to indicate the boundary layer height variability associated with atmospheric fluctuations, which is larger than the vertical resolution. Based on these considerations, we don't see any physical reason for having the standard deviation and the mean of this measured quantity rounded up to the closest available range bin, as long as these values are expressed with the same number of significant digits as the vertical resolution. By the way the mean boundary layer height (1290 m) is an exact multiple

value of the range resolution (7,5 m), so for this mean value rounding up to the closest available range bin is not required; on the other hand, the boundary layer height standard deviation (± 77 m) is 2 m off an exact multiple value of the range resolution (75 m). However, in order to remove any residual skepticism by the referee, we corrected the standard deviation value from ± 77 m to ± 75 m both times this was appearing in the text (i.e. page 2, line 6 and page 19, line 4), this change having negligible effects on the results reported in this paper.

Pag 2 Line 30 please read "unstable"

Corrected as requested by the referee.

Pag 7 Line 1-3. It is not clear if the calibration coefficients were calculated globally or for each single radiosonde launch.

As already specified in the text, during HOPE the Raman lidar was calibrated based on the comparison with the radiosondes launched approximately 4 km away. We considered all clear sky radiosonde launches coincident with lidar operation (sixty in total), thus determining sixty values for each calibration coefficient. A mean value for the calibration coefficient was then estimated from these sixty values. This is now more clearly specified in the text, where the corresponding sentence has been modified as follows: "All clear sky radiosonde launches coincident with lidar operation (sixty in total) were considered, thus determining sixty distinct values for each calibration coefficient. A mean value for each calibration coefficient was then estimated and used throughout the HOPE period."

Page 11 Line 25, and in all the manuscript: please change leakage with "cross-talk".

We agree with the referee that the term "cross-talk" is more appropriate than the term "leakage" to describe the optical effect taking place in our Raman lidar receiving system. In fact, as most Dictionaries confirm (among others, Oxford Dictionaries, Collins English Dictionary, American Heritage Dictionary), the term "leakage" is meant to indicate the "undesired escape or loss of a quantity, such as electromagnetic radiation, electric charges, etc.", the lost quantity not being necessarily transferred to a different channel, while "cross-talk" indicates the "unwanted transfer of signal from one channel to another". In our case, we don't have an escape or loss of a portion of the elastic signal photons entering the elastic channel, with a consequent reduction of the strength of the sampled elastic signal, but the undesired entrance of a small portion of the elastic signal photons (which would not be entering the elastic channel in any case) into the low-quantum number rotational Raman channel. As a result of this, the amplitude of the sampled elastic signal is not reduced, but indeed there is an undesired transfer of elastic signal to the low-quantum number rotational Raman channel. The term "leakage" has been substituted with the term "cross-talk" throughout the text.

Page 13 Line 18 Most of the backscattering values are less than $1 \cdot 10^{-6} \text{ m}^{-1} \text{ sr}^{-1}$

The referee is right: most particle backscattering values within the boundary layer are less than $1 \cdot 10^{-6} \text{ m}^{-1} \text{ sr}^{-1}$ and not in excess of this value, as erroneously stated in the text. Values were erroneously reported as a result of an oversight in reading the color scale. Instead, particle backscattering values are between 0.3 and $1.4 \cdot 10^{-6} \text{ m}^{-1} \text{ sr}^{-1}$. This oversight has been corrected in the text, where the corresponding sentence now reads: "The figure reveals the presence of a significant aerosol loading within the boundary layer (with values of β_{par} in the range $0.3\text{-}1.4 \cdot 10^{-6} \text{ m}^{-1} \text{ sr}^{-1}$), tracing the presence ...".

Page 18 Line 21 I suggest adding two more works that will give an exhaustive view of PBL retrieval methods by lidar means. The works I suggest are: Haeffelin, M., Angelini, F., Morille, Y. et al. Boundary-Layer Meteorol (2012) 143: 49. doi:10.1007/s10546-011-9643-z and Conor Milroy,

Giovanni Martucci, Simone Lolli, et al., “An Assessment of Pseudo-Operational Ground-Based Light Detection and Ranging Sensors to Determine the Boundary-Layer Structure in the Coastal Atmosphere,” *Advances in Meteorology*, vol. 2012, Article ID 929080, 18 pages, 2012. doi:10.1155/2012/929080

The two additional papers suggested by the referee are now cited in the manuscript and have been added to the reference list.

Pag 18 Line 27 see remarks in the abstract section

Here the referee is pointing to the mean and standard deviation values for the CBL height published by other authors (Muppa *et al.*, 2016) and which are cited here only for comparison with ours. We believe these values should appear here as they appeared in the literature.

Pag 24 Line 10 Due to the intrinsic properties of lidar measurements, are the retrieved variables (water vapor and temperature) normal distributed (and then does it make sense to define 3rd and 4th moment?) Please clarify

A geophysical time series such as water vapour and temperature fluctuations are generally not normal distributed because these are determined by non-linear turbulent processes. It is exactly our goal to specify the distribution of the turbulent fluctuations because they give us unique insight in the turbulent process understanding and its parameterization in models. The third- and fourth-order moment are variables closely related to skewness and kurtosis, respectively. Specifically, the third-order moment quantifies the degree of asymmetry of the distribution of the considered atmospheric variable fluctuations, with positive values indicating a right-skewed distribution (with the mode smaller than the mean) and negative values indicating a left-skewed distribution (with the mode larger than the mean). Analogously, the fourth-order moment indicates the steepness of the distribution and the width of its peak. While the vertical profiles of skewness and kurtosis for water vapour mixing ratio and temperature fluctuations are reported in the paper (page 26 and figure 13), the paper primarily focuses on the discussion on the third- and fourth-order moment of these atmospheric variables fluctuations. The choice of focusing the discussion primarily on the third- and fourth-order moment is motivated by the fact that the third- and fourth-order moments have more regular vertical profiles - characterized by a smaller number of spikes and spurious fluctuations - than skewness and kurtosis. This is because skewness and kurtosis are obtained from the third- and fourth-order moment through normalization by the atmospheric variance and, consequently, spikes and spurious fluctuations may occur in those altitude regions of the convective boundary layer where atmospheric variance has very small values. However, in the entrainment zone, atmospheric variance for both water vapour mixing ratio and temperature is characterized by large values and this makes skewness and kurtosis for both atmospheric variables very stable and accurately determinable within this altitude region. In the entrainment zone values of skewness for both humidity and temperature fluctuations are found to be large, as expected for fluctuations strongly deviating from a normal distribution. This aspect is now more clearly specified in the text, where the corresponding sentences have been changed as follows: in page 26, lines 7-12, “Values of water vapour mixing ratio skewness are in very good agreement with those reported by Wulfmeyer *et al.*, 2010, with positive values (up to 1.5) in the lower portion of the CBL (up to 800 m, i.e. $z/z_i=0.65$), with negative values (down to -1) in the middle and upper portion of the CBL ($800 < z < 1290$ m, i.e. $0.65 < z/z_i < 1.00$). Large positive values are found within the entrainment zone and just above the CBL top (with a maximum of approx. 5 at 1400 m, i.e. $z/z_i=1.15$), which testifies the presence of humidity fluctuations strongly deviating from a normal distribution”; and in page 26, lines 20-26, “Temperature skewness has a negative peak (~ -4) at 500 m, i.e. $z/z_i=0.4$, positive peaks (~ 8 and 4) at 890 and 1100 m (i.e. $z/z_i=0.7$ and $z/z_i=0.85$), respectively, and negative values within the entrainment zone and just above the CBL top (with a peak value of ~ -7 at 1460 m, i.e. $z/z_i=1.13$), in in good agreement with measurements reported by Behrendt *et al.* (2015, 40-120 s) for the

nearby site of Hambach, but a different case study. Again, values of skewness within the entrainment zone and just above the CBL top are found to be large, as expected for temperature fluctuations strongly deviating from a normal distribution”. Furthermore, as specified in the Abstract (page 2, line 16) and in Section 4.3 (page 26-27, lines 27-3), in the upper portion of the CBL, water vapour and temperature kurtosis are found to have values close to 3, which is an indication of normally distributed humidity and temperature fluctuations (mesokurtic-Gaussian distribution), while in the entrainment zone and above the CBL top water vapour and temperature kurtosis show values as large as 18 as a result of the presence of humidity and temperature fluctuations strongly deviating from a normal distribution. The corresponding paragraph has been changed as follows: “Values of kurtosis in the upper portion of the CBL (in the height interval 1160-1280 m) are in the range 2.76-3.83, with a mean value of 3.36, for water vapour mixing ratio fluctuations, while they are in the range 2.68-3.45, with a mean value of 3.17, for temperature fluctuations. These values indicate normally distributed (mesokurtic-Gaussian distribution) humidity and temperature fluctuations in the upper portion of the CBL (Wulfmeyer *et al.*, 2010; Turner *et al.* 2014a, Behrendt *et al.*, 2015, Muppa *et al.*, 2016). In the entrainment zone and above the CBL top, values of water vapour mixing ratio and temperature kurtosis are found to be large (up to 18) as a result of the presence of humidity and temperature fluctuations strongly deviating from a normal distribution.”

For what concerns the reference to the “intrinsic properties of lidar measurements”, here we believe the referee refers to the application of Poisson statistics to lidar signal photon counts. In fact, photon counts are measured by our Raman lidar through a photon counting unit, while “virtual” counts are measured through an analog module (e.g. Newsom *et al.*, 2009). For lidar measurements carried out in the convective boundary layer, as those presented in this paper, the number of photon counts and “virtual” counts detected by the receiving system is large enough to allow the approximation of count statistics with a Gaussian distribution. In fact, for an increasing number of photons, Poisson distribution becomes more and more symmetric, and begins to resemble a Gaussian shape. The Gaussian distribution is found to adequately approximate the Poisson distribution when the mean number of photons is in excess of 10 (among others, Russo, 2007). Higher moments of the noise distribution can also be studied with the tools introduced in Lenschow *et al.* 2000. Our current results do not indicate a significant deviation of the noise distribution from Gaussian.

Figure 4, 5 and 7 are not very clear and the resolution should be improved.

In these figures we improved the graphical resolution to make them clearer.

References

Newsom, R. K, Turner, D. D., Mielke, B., Clayton, M., Ferrare, R., Sivaraman, C.: The use of simultaneous analog and photon counting detection for Raman lidar. *Appl. Opt.*, 48, 3903–3914, doi: 10.1364/AO.48.003903, 2009.

Russo, F.: An Investigation of Raman Lidar Aerosol Measurements and their Application to the study of the Aerosol Indirect Effect, PhD dissertation, Physics Department, University of Maryland, Baltimore County, 2007.

Wulfmeyer, V., Muppa, S., Behrendt, A., Hammann, E., Späth, F., Sorbjan, Z., Turner, D.D., and Hardesty, R.M.: Determination of convective boundary layer entrainment fluxes, dissipation rates, and the molecular destruction of variances: Theoretical description and a strategy for its confirmation with a novel lidar system synergy, *J. Atmos. Sci.*, 73 (2), 667-692, doi: 10.1175/JAS-D-14-0392.1, 2016.

Wulfmeyer, W., and Turner, D. D.: Land-Atmosphere Feedback Experiment (LAFE) Science Plan, DOE/SC-ARM-16-038, www.arm.gov/publications/programdocs/doe-sc-arm-16-038.pdf, 2016.

1 **Characterization of Boundary Layer Turbulent Processes by the Raman Lidar**
2 **BASIL in the frame of HD(CP)² Observational Prototype Experiment**

3
4 **Paolo Di Girolamo¹, Marco Cacciani², Donato Summa¹, Andrea Scoccione², Benedetto De Rosa¹,**
5 **Andreas Behrendt³, Volker Wulfmeyer³**

6
7 [1] Scuola di Ingegneria, Università degli Studi della Basilicata, Viale dell'Ateneo Lucano n. 10, 85100
8 Potenza – Italy, email: digirolamo@unibas.it

9 [2] Dipartimento di Fisica, Università di Roma “La Sapienza”, Piazzale Aldo Moro, n. 2, 00100 Roma –
10 Italy, email: marco.cacciani@uniroma1.it

11 [3] Institut für Physik und Meteorologie, Universität Hohenheim, Hohenheim – Germany, email:
12 andreas.behrendt@uni-hohenheim.de, volker.wulfmeyer@uni-hohenheim.de

13
14 **Abstract**

15 Measurements carried out by the University of BASILicata Raman lidar system (*BASIL*) are reported to
16 demonstrate the capability of this instrument to characterize turbulent processes within the convective
17 boundary layer (CBL). In order to resolve the vertical profiles of turbulent variables, high resolution
18 water vapour and temperature measurements, with a temporal resolution of 10 s and a vertical
19 resolution of 90 m and 30 m, respectively, are considered. Measurements of higher-order moments of
20 the turbulent fluctuations of water vapour mixing ratio and temperature are obtained based on the
21 application of auto-covariance analyses to the water vapour mixing ratio and temperature time series.
22 The algorithms are applied to a case study (11:30-13:30 UTC, 20 April 2013) from the High Definition
23 Clouds and Precipitation for Climate Prediction (HD(CP)²) Observational Prototype Experiment
24 (HOPE), held in Western Germany in the spring 2013. A new correction scheme for the elastic-signal
25 | leakage-cross-talk into the low-quantum number rotational Raman signal is applied. The noise errors are
26 small enough to derive up to fourth-order moments for both water vapour mixing ratio and temperature
27 fluctuations.

28 To the best of our knowledge, *BASIL* is the first Raman lidar with a demonstrated capability to
29 simultaneously retrieve daytime profiles of water vapour turbulent fluctuations up to the fourth order
30 throughout the atmospheric CBL, this capability being combined with the one to also measure daytime

1 profiles of temperature fluctuations up to the fourth order. These measurements, in combination with
2 measurements from other lidar and in-situ systems, are important to verify and possibly improve
3 turbulence and convection parameterization in weather and climate models at different scales down to
4 the grey zone (grid increment ~ 1 km) (Wulfmeyer et al. 2016).

5 For the considered case study, which represents a well-mixed and quasi-stationary CBL, the mean
6 boundary layer height is found to be 1290 ± 757 m a.g.l. Values of the integral scale for water vapour and
7 temperature fluctuations at the top of the CBL are in the range of 70-125 s and 75-225 s, respectively;
8 these values are much larger than the temporal resolution of the measurements (10 s), which testifies
9 that the temporal resolution considered for the measurements is sufficiently high to resolve ~~turbulenee~~
10 turbulent processes down to the inertial sub-range and consequently resolve the major part of the
11 turbulent fluctuations. Peak values of all moments are found in the interfacial layer in the proximity of
12 the top of the CBL. Specifically, water vapour and temperature second-order moment (variance) has a
13 maximum value of $0.29 \text{ g}^2\text{kg}^{-2}$ and 0.26 K^2 , respectively, water vapour and temperature third-order
14 moment has a peak value of $0.156 \text{ g}^3\text{kg}^{-3}$ and -0.067 K^3 , respectively, while water vapour and
15 temperature fourth-order moment has a maximum value of $0.28 \text{ g}^4\text{kg}^{-4}$ and 0.24 K^4 , respectively. Water
16 vapour and temperature kurtosis have values of ~ 3 in the upper portion of the CBL~~the entrainment zone~~,
17 which indicate normally distributed humidity and temperature fluctuations. Reported values of the
18 higher-order moments result to be in good agreement with previous measurements at different locations,
19 thus providing confidence on the possibility to use them for turbulence parameterization in weather and
20 climate models.

21 In the determination of the temperature profiles, particular care was dedicated to minimize potential
22 effects associated with elastic signal ~~leakage-incross-talk into~~ the rotational Raman signals. For this
23 purpose, a specific algorithm was defined and tested to identify and remove signal ~~leakages-cross-talk~~
24 and to assess the residual systematic uncertainty affecting temperature measurements after correction.
25 The application of this approach confirms that for the present Raman lidar system the ~~leakage-cross-talk~~
26 factor keeps constant with time, and consequently an appropriate assessment of its constant value allows
27 for a complete removal of the leaking elastic signal from the rotational Raman lidar signals at any time
28 (with a residual error on temperature measurements after correction not exceeding 0.16 K).

30 **1 Introduction**

31 Water vapour and temperature are key meteorological variables playing a major role in the definition of
32 the thermodynamic state of the atmosphere (Wulfmeyer *et al.* 2015). This is particularly true in the

1 | convective boundary layer, the unstable~~ly~~ stratified boundary layer developing in the lower troposphere
2 during the day, dominated by buoyant turbulence generation as a result of strong surface solar heating
3 (Garratt, 1992). Entrainment processes at the top of the CBL are controlled by temperature (capping)
4 inversion in the interfacial layer, ultimately influencing the vertical transport of humidity in the free
5 troposphere (Mahrt 1991; Sorbjan 1996; Sullivan *et al.* 1998, Wulfmeyer *et al.* 2016). Accurate
6 measurements of water vapour and temperature from the surface to the entrainment zone at the top of
7 the CBL are therefore essential for improving weather forecasting (Dierer *et al.*, 2009), reanalyses
8 (Bengtsson *et al.*, 2004), and regional climate simulations (Milovac *et al.* 2016).

9 Measurements of higher-order moments of moisture and temperature fluctuations provide unique and
10 essential information for the characterization of turbulent processes within the convective boundary
11 layer (CBL). Water vapour and temperature variances are key variables in turbulence, convection, and
12 cloud parameterizations considered in weather and climate models (e.g., Stull, 1988; Berg and Stull,
13 2005; Gustafson and Berg, 2007). Within the CBL, water vapour variance increases with height,
14 achieving a maximum at the top of the CBL due to the mixing of moist air in the updrafts with drier air
15 from above the CBL (Wulfmeyer 1999a,b; Kiemle *et al.*, 2007). The water vapour variance profile can
16 also be used to estimate the CBL height and characterize its internal structure by exploiting the tracing
17 capabilities of atmospheric water vapour (among others, Wulfmeyer *et al.*, 2010; Turner *et al.*, 2014a,b).
18 Furthermore, water vapour skewness and kurtosis are found to be characterized by an appreciable
19 vertical variability within the CBL, which changes patterns during different phases of the CBL
20 evolution (Couvreaux *et al.*, 2005, 2007).

21 Atmospheric turbulent processes within the CBL have been studied for decades based on the use of in-
22 situ sensors (among others, Lenschow and Kristensen, 1985, Kalthoff *et al.*, 2011). However, lidar
23 systems, on the basis of their capability to provide high space and time resolution and accurate
24 measurements of atmospheric water vapour and temperature, have nowadays reached the level of
25 maturity needed to investigate the relevant atmospheric processes and enable measurements of turbulent
26 variables within the CBL (among others, Eberhard *et al.*, 1989; Frehlich and Cornman, 2002). The
27 major advantage of the lidar techniques is represented by their capability to characterize turbulent
28 variables from the proximity of the surface up to interfacial layer and above. Additionally, lidar systems
29 can be operated from different platforms and, when applied from ground-based platforms, can provide
30 excellent long-term statistics. This is also necessary for reducing sampling error which are usually
31 larger for ground-based than for airborne measurements.

1 For the characterization of water vapour turbulent fluctuations, the DIAL and Raman lidar techniques
2 have demonstrated to have the time and vertical resolution, as well as the accuracy, needed to
3 characterize turbulent processes within the CBL (Wulfmeyer, 1999a,b; Kiemle *et al.*, 2007; Wulfmeyer
4 *et al.*, 2010, Turner *et al.* 2014a; Muppa *et al.*, 2016). Profiles of second- to fourth-order moments of
5 turbulent temperature fluctuations in the convective boundary layer have been reported for the first time
6 by Behrendt *et al.* (2015) based on the application of the rotational Raman lidar (RRL) technique
7 (Behrendt and Reichardt, 2000; Behrendt *et al.*, 2002; Di Girolamo *et al.*, 2004, 2006; Behrendt, 2005;
8 Radlach *et al.*, 2008; Hammann *et al.*, 2015a, Hammann and Behrendt, 2015). The present
9 measurements have been carried out by the Raman lidar system *BASIL*, exploiting its capability to
10 perform high-resolution and accurate measurements of atmospheric temperature and water vapour, both
11 in daytime and night-time, based on the application of the rotational and vibrational Raman lidar
12 techniques in the UV, respectively (Di Girolamo *et al.*, 2004, 2006, 2009a; 2016a, Bhawar *et al.*, 2011).
13 These measurements allow for the determination of the vertical profiles of the turbulent fluctuation of
14 these two atmospheric variables up to the fourth order throughout the atmospheric CBL in daytime with
15 limited uncertainty. Results from this system are obtained based on the application of the approach
16 introduced by Lenschow *et al.* (2000), which allows for estimating higher-order moments of turbulent
17 variables in the presence of noisy data. Measurements of water vapour turbulent fluctuations by Raman
18 lidar had been demonstrated by Wulfmeyer *et al.* (2010), based on the use of the data from the
19 Atmospheric Radiation Measurement (ARM) Raman lidar. However, these authors came to the
20 conclusion that the noise errors affecting the ARM Raman lidar water vapour mixing ratio
21 measurements for the considered case study were too large to derive fourth-order moments with
22 sufficient accuracy. Thus, to the best of our knowledge, *BASIL* is the first Raman lidar with a
23 demonstrated capability to accurately retrieve simultaneous daytime profiles of water vapour and
24 temperature turbulent fluctuations up to the fourth order throughout the atmospheric CBL. The main
25 aim of this paper is to provide a detailed characterization of the performances of the Raman lidar *BASIL*
26 and demonstrate that profiles of turbulent variables can be determined throughout the CBL with
27 sufficient accuracy. For this purpose measurements from the High Definition Clouds and Precipitation
28 for Climate Prediction (HD(CP)2) Observational Prototype Experiment (HOPE), held in Western
29 Germany in spring 2013, are considered.

30 The paper outline is the following. Section 2 provides a description of the experimental setup, with
31 details on the data processing and the error analyses; this section also describes the correction scheme
32 considered for removing the elastic-signal ~~cross-talk into leakage in~~ the low-quantum number rotational
33 Raman signal and the uncertainties associated with this approach. Section 3 provides a brief overview

1 on the HOPE field campaign and illustrates the criteria considered for the selection of the case study;
2 this section also illustrates the ~~the~~-time-height cross-sections of the water vapour mixing ratio and
3 temperature data considered for the turbulence analysis, providing remarks on the meteorological
4 conditions occurring during this period. Section 4 provides a brief description of the methodology
5 considered for the turbulence analysis and illustrates the results achieved in terms of vertical profiles of
6 turbulent variables. Finally, section 5 summarizes all results and provides some indications for possible
7 future work.

8

9 **2 Experimental setup**

10 **2.1 System Set up and derivation of mixing-ratio and temperature profiles**

11 Prior to HOPE, the University of BASILicata Raman lidar system (*BASIL*) underwent a substantial
12 upgrade aimed to improve its overall performances in terms of measurement precision and vertical and
13 temporal resolution. These setup modifications will be described in a separate forthcoming paper (Di
14 Girolamo *et al.*, 2016b). *BASIL* is a ground-based Raman lidar hosted in a transportable sea-tainer. The
15 major feature of *BASIL* is represented by its capability to perform high-resolution and accurate
16 measurements of the vertical profiles of atmospheric temperature and water vapour, both in daytime and
17 night-time, based on the application of the rotational and vibrational Raman lidar techniques in the UV
18 (Di Girolamo *et al.*, 2004, 2006, 2009a; 2016a, Bhawar *et al.*, 2011). Besides temperature and water
19 vapour, *BASIL* is also capable of providing measurements of the vertical profiles of particle backscatter
20 at 354.7, 532 and 1064 nm, particle extinction at 354.7 and 532 nm and particle depolarization at 354.7
21 and 532 nm (Griaznov *et al.*, 2007; Di Girolamo *et al.*, 2009b, 2012a, 2012b). *BASIL* is built around a
22 Nd:YAG laser source, equipped with second and third harmonic generation crystals, capable of emitting
23 pulses at 354.7 nm, 532 nm and 1064 nm, which are simultaneously transmitted in the atmosphere along
24 the zenith. The receiver includes a large-aperture telescope in Newtonian configuration, with a 45 cm
25 diameter primary mirror and a focal length of 2.1 m, and two small-aperture telescopes (50 mm
26 diameter lenses). The radiation collected by the large-aperture telescope is split into eight portions by
27 means of dichroic or partially reflecting mirrors: specifically, two portions are fed into the detection
28 channels used for temperature measurements (at 354.3 and 352.9 nm for the low- and high-quantum
29 number rotational Raman signals, $P_{LoJ}(z)$ and $P_{HiJ}(z)$, respectively), while two other portions are sent
30 to the water vapour (at 407.5 nm) and molecular nitrogen Raman channels (at 386.7 nm); corresponding
31 signals are $P_{H_2O}(z)$ and $P_{N_2}(z)$, respectively, in what follows. Another two portions of the collected
32 radiation are fed into the 354.7 and 532 nm elastic channels. A fraction of the signal entering the 354.7

1 nm channel is split into two additional portions to allow the detection of the parallel and cross-polarized
 2 elastic signals, which are used for the determination particle depolarization. Signal selection is
 3 performed by means of narrowband interference filters, whose specifications were defined in Di
 4 Girolamo *et al.* (2004, 2009a).

5 The water vapour mixing ratio m can be obtained from the power ratio of water vapour to molecular
 6 nitrogen vibrational Raman signals ($m(z) = K(z) \cdot (P_{H_2O}(z)/P_{N_2}(z))$), where $K(z)$ is a calibration factor
 7 obtained by multiplying several height-dependent correction terms and a height-independent
 8 calibration term (e.g., Whiteman, 2003). The height-dependent correction terms included $K(z)$ are a
 9 differential transmission term, accounting for the different atmospheric transmission by molecules and
 10 aerosols at the two wavelengths corresponding the water vapour and molecular nitrogen Raman signals,
 11 and a term associated with the use of narrowband interference filters and the consequent temperature
 12 dependence of H₂O and N₂ Raman scattering signals selected by these filters. The height-independent
 13 calibration factor is finally obtained by the multiplication of the above mentioned signal ratio by the
 14 height-dependent correction terms included $K(z)$ and the comparison of this quantity with simultaneous
 15 and co-located mixing ratio measurements from different sensors (e.g., from radiosondes, microwave
 16 radiometers, GPS tomography, etc.).

17 Based on the application of the pure rotational Raman lidar technique, atmospheric temperature is
 18 obtained from the power ratio of high-to-low quantum number rotational Raman signals $Q(T)$ through
 19 the application of the analytical expression:

$$20 \quad Q(z) = P_{HiJ}(z)/P_{LoJ}(z) = \exp(\alpha/T(z) + \beta) \quad (1)$$

21 with α and β being two calibration constants. Thus:

$$22 \quad T(z) = \frac{\alpha}{\ln[Q(z)] - \beta} \quad (2)$$

23 These two calibration constants can be determined through the comparison of the lidar signal ratio with
 24 simultaneous and co-located temperature measurements from different sensors (e.g., ~~from again,~~
 25 radiosondes, microwave radiometers, ~~GPS tomography,~~ etc.). The above considered analytical
 26 expression relating $Q(z)$ to $T(z)$ is not the only possible expression, but it is probably the simplest and
 27 implies the smallest number of calibration constants. Other more complex analytical expression have
 28 been considered in literature (Behrendt and Reichardt, 2000; Di Girolamo *et al.*, 2004; Behrendt *et al.*,
 29 2015). However, the systematic error associated with assuming the above calibration function to be
 30 valid for a large portion of the rotational Raman spectrum is found to have a typical amplitude of 0.2 K,

1 which is not relevant for the purposes of the present study (see Wulfmeyer *et al.*, 2016 for an
2 assessment of the effects of systematic errors on turbulence measurements).

3 During HOPE, water vapour mixing ratio and temperature measurements by *BASIL* were both
4 calibrated based on the comparison with simultaneous radiosondes, which were launched from the
5 nearby supersite UHOH-KIT, located in Hambach, approx. 4 km E-SE. All clear sky radiosonde
6 launches coincident with lidar operation (sixty in total) were considered, thus determining sixty distinct
7 values for each calibration coefficient. A mean value for each calibration coefficient was then estimated
8 and used throughout the HOPE period. ~~Mean calibration coefficients for both water vapour mixing ratio
9 and temperature measurements were estimated by comparing *BASIL* and radiosonde profiles for all
10 radiosondes launched at times when *BASIL* was operating (approximately 60 comparisons).~~ The
11 comparisons were carried out in a vertical region with an extent of 1 km located above the boundary
12 layer. This selection allows for minimizing the air mass differences related to the physical distance
13 between the lidar and the radiosonde. The variability of the calibration coefficients was found to be very
14 limited throughout the duration of the field campaign, with single calibration values showing very small
15 deviations from the mean values. For example, for what concerns water vapour measurements, the
16 standard deviation of single calibration values from the mean calibration coefficient was found to not
17 exceed 5 %.

18 As specified above, *BASIL* underwent an upgrade before HOPE which allowed for obtaining a
19 substantial improvement of the overall performances in terms of both measurement precision and
20 vertical and temporal resolution. The upgrade included a modification of the optical layout of the
21 Nd:YAG laser source, which allowed to achieve a 65 % increase of its emitted power in the UV (from
22 an original value of 6 W, single pulse energy of 300 mJ @ 20 Hz, to a final value of 10 W, with a single
23 pulse energy of 500 mJ @ 20 Hz). The upgrade also included the implementation of a new sampling
24 system (with double signal acquisition mode, i.e. both analog & digital) in some of the measurement
25 channels allowing to acquire daytime and nighttime lidar signals with a maximum vertical and temporal
26 resolution of 7.5 m and 1-10 sec, respectively. In signal pre-processing, four adjacent data points are
27 binned together to reduce statistical fluctuations of the signals, this increasing the vertical step between
28 adjacent data points to 30 m.

29 30 **2.2 Determination of noise errors**

31 In order to characterize the quality of water vapour mixing ratio and temperature measurements, an
32 accurate assessment of noise error is necessary. Noise error is quantified as the root-square of the noise

1 variance (i.e. the noise standard deviation). Profiles of noise error affecting water vapour mixing ratio
2 and temperature measurements are illustrated in figure 1. Specifically, figure 1a illustrates the water
3 vapour mixing ratio absolute error (expressed in g kg^{-1}), figure 1b illustrates the water vapour mixing
4 ratio relative error (expressed in %), while figure 1c illustrates the temperature absolute error (expressed
5 in K). The figure shows the noise error profiles estimated based on the application of the auto-
6 covariance method (described in detail in sub-section 4.1). More specifically, noise error assessments
7 have been performed considering two options for temporal and vertical resolution: a higher resolution
8 configuration, with a time resolution of 10 s and a vertical resolution of 90 m and 30 m for water vapour
9 mixing ratio and temperature, respectively (this is the selection considered for the turbulence
10 measurements); and a lower resolution configuration, with a time resolution of 150 s and a vertical
11 resolution of 5 min, which is the selection considered for the data set generated and uploaded to the
12 HOPE archive (primarily used for verification purposes, process studies and data assimilation). For the
13 first selection, the statistical error affecting water vapour mixing ratio measurements is smaller than 0.6
14 g kg^{-1} (or 50 %) up to 1.4 km, while the statistical error affecting temperature measurements is smaller
15 than 1 K up to 1.8 km. For the second selection, the statistical error affecting water vapour mixing ratio
16 measurements is smaller than 0.1 g kg^{-1} (or 15 %) up to 1.8 km, while the statistical error
17 affecting temperature measurements is smaller than 0.8 K up to 3 km. The above listed performances of
18 *BASIL* in terms of water vapour mixing ratio measurements result to be comparable with those reported
19 for the ARM Raman lidar (Wulfmeyer *et al.*, 2010, also 0.6 g kg^{-1} at 1.4 km), considering the same time
20 and vertical resolution. Same is true for the above listed performances of *BASIL* in terms of temperature
21 measurements, which indicate statistical uncertainties with values similar to those reported for the ARM
22 Raman lidar (Newsom *et al.*, 2013). The above quantified errors are used to derive - by means of error
23 propagation - the noise error profiles of the higher-order moments. An overview of these equations is
24 given in Wulfmeyer *et al.*, (2016).

25 In practice, water vapour mixing ratio and temperature profiles can be derived with different vertical
26 and temporal resolutions depending on the considered application. Vertical and temporal resolutions can
27 be traded-off with measurement precision, with random error affecting water vapour mixing ratio and
28 temperature measurements being inversely proportional to the square root of both vertical and temporal
29 resolution. Consequently, the consideration of the high temporal and vertical resolutions (10 sec, 30-90
30 m, respectively) needed for the characterization of turbulence processes translates into a lower
31 measurement precision (and consequently a larger statistical error). As a result of this, the
32 corresponding statistical error affecting daytime water vapour mixing ratio and temperature

1 measurements is smaller than 100 % and 1 K, respectively, up to 2 km (figure 1), these performances
 2 being well suited for lidar measurements finalized to the characterization of turbulent variables.

3 Figure 1 also includes the error profiles obtained with the application of Poisson statistics to signal
 4 photon counts. Signal photon counts are directly measured by the photon counting unit; “virtual” counts
 5 can also be obtained from the signals measured by the analog module (Newsom *et al.*, 2009). In order to
 6 get an estimate of the error affecting water vapour mixing ratio and temperature measurements through
 7 Poisson statistics, it is necessary to first apply Poisson statistics to the photon counts of the individual
 8 lidar signals contributing to the measurements and then, through error propagation, compute the overall
 9 error affecting the measured atmospheric variables. The error propagation expression is different for
 10 water vapour mixing ratio and temperature measurements as different are the analytical expressions
 11 relating the individual signals to the two measured parameters. For water vapour mixing ratio
 12 measurements the application of error propagation yields the expression (Di Girolamo *et al.*, 2009a):

$$13 \quad \frac{\Delta x_{H_2O}(z)}{x_{H_2O}(z)} = \sqrt{\frac{P_{H_2O}(z) + bk_{H_2O}}{P_{H_2O}^2(z)} + \frac{P_{N_2}(z) + bk_{N_2}}{P_{N_2}^2(z)}} \quad (3)$$

14 where the terms bk_{H_2O} and bk_{N_2} represent the sky background signal (primarily associated with solar
 15 irradiance) collected in the water vapour and molecular nitrogen channels, respectively. Expression (3)
 16 provides the relative statistical error (in percentage if multiplied for 100), while the absolute statistical
 17 error can be obtained by multiplying expression (3) for $x_{H_2O}(z)$. The mean photon number for the 10
 18 sec water vapour and molecular nitrogen vibrational Raman signals, $P_{H_2O}(z)$ and $P_{N_2}(z)$, displayed in
 19 figure 2, are found to vary featuring a maximum around 800 m of approx. 1500 and 12000 counts,
 20 respectively, and progressively decreasing down to 0 and approx. 20 counts, respectively, around 10 km
 21 (after background subtraction). Here the mean photon number is intended as the average of all 10 sec
 22 signal profiles collected over the period 11:30-13:30 UT on 20 April 2013. Figure 2 also shows the
 23 mean photon number for the 10 sec 354.7 nm elastic signal, $P_{354.7}(z)$, which has a maximum of approx.
 24 2200 counts around 800 m and progressively decreases down to 2 counts around 10 km.

25 For temperature measurements the application of error propagation yields the expression (Behrendt *et*
 26 *al.*, 2002, 2015, Di Girolamo *et al.*, 2006, 2009a):

$$27 \quad \Delta T(z) = \frac{\partial T(z)}{\partial R} R(z) \sqrt{\frac{P_{LoJ}(z) + bk_{LoJ}}{P_{LoJ}^2(z)} + \frac{P_{HiJ}(z) + bk_{HiJ}}{P_{HiJ}^2(z)}} \quad (4)$$

1 where the terms bk_{LoJ} and bk_{HiJ} represent the sky background signal collected in the low- and high-J
2 rotational Raman channels, respectively. The quantity $\partial T(z)/\partial R$ can be estimated based on the
3 application of the calibration procedure mentioned above. The mean photon number for the 10 sec low
4 and high quantum number rotational Raman signals, $P_{LoJ}(z)$ and $P_{HiJ}(z)$, also displayed in figure 2, is
5 found to vary featuring a maximum of approx. 4500 and 3500 counts, respectively, at 800 m, and
6 progressively decreasing down to 8 and 4 counts respectively, around 10 km. Figure 2 also shows the
7 temperature sensitivity of RRL measurement technique, i.e. the quantity $\partial R(z)/\partial T$, which is found to
8 vary between $0,06 \text{ K}^{-1}$ at surface level to approx. $0,03 \text{ K}^{-1}$ at 10 km, and the power ratio of high-to-low
9 quantum number rotational Raman signals, $R(z)$, which is found to vary between approx. 0,8 at surface
10 level to approx. 0,3 at 10 km. The large values of the measurement sensitivity ($\partial R(z)/\partial T$) contribute to
11 the small random errors affecting the reported temperature measurements.

12 The terms bk_{H_2O} and bk_{N_2} in expression (3) and the terms bk_{LoJ} and bk_{HiJ} in expression (4) can be
13 determined considering the photon-counting signals at very high heights, this portion of the signals
14 being characterized by negligible contribution from laser backscatter photons and being typically
15 attributable to sky background radiation and intrinsic detector noise, the former being much larger than
16 the latter, especially for daytime operation. For the reported measurements, values of bk_{H_2O} and
17 bk_{N_2} are found to be approx. 11000 and 8000 counts, respectively, while values of bk_{LoJ} and bk_{HiJ} are
18 found to be approx. 200 and 1000 counts, respectively.

19 It is to be noticed that the auto-covariance analysis specifies the total statistical noise, while Poisson
20 statistics accounts only for its shot noise contribution, i.e. the contribution associated with the discrete
21 nature of the photons sampled by photon counting devices. Consequently, the application of Poisson
22 statistics to signal photon counts leads to an underestimation of the total statistical noise (Wulfmeyer *et*
23 *al.*, 2010, Behrendt *et al.*, 2015). Figure 1 reveals that noise error estimates obtained through the
24 application of Poisson statistics are in good agreement with estimates obtained through the auto-
25 covariance approach. Specifically, Poisson statistics accounts for approximately 75 % of the total
26 statistical noise affecting the measurement of water vapour mixing ratio and temperature. In more detail,
27 Poisson statistics accounts for 60 to 80 % of the total statistical noise affecting water vapour mixing
28 measurements, with a mean value of 74.5 %, while it accounts for 60 to 90 % of the total statistical
29 noise affecting temperature measurements, with a mean value of 78.0 %. This confirms that photon shot
30 noise represents the main contribution to the total statistical noise, but other statistical error sources,
31 usually very small, may also contribute.

1 As a result of the above described upgrades, *BASIL* performances in terms of the atmospheric variables
2 of interest for the purposes of this paper, extrapolated at higher heights based on the application of
3 Poisson statistics, are as follows. For water vapour mixing ratio measurements, the typical daytime
4 statistical error (precision) is smaller than 20 % up 3 km and smaller than 100 % up 4.5 km, while the
5 typical nighttime statistical error is smaller than 2 % up 3 km and smaller than 20 % up 9 km, based on
6 an integration time of 5 min and a vertical resolution of 150 m. The statistical error
7 affecting temperature measurements for daytime operation is typically smaller than 0.5 K up to 3 km
8 (figure 1) and smaller than 1.5 K up to 4.5 km, while for night-time operation is typically smaller
9 than 0.4 K up to 3 km (figure 1) and smaller than 1 K up to 6.5 km. These error values are consistent
10 with the performances of the ARM water vapour Raman lidar (Wulfmeyer *et al.*, 2010; Turner *et al.*,
11 2014a).

12

13 **2.3 Systematic errors**

14 **2.3.1 Time independent systematic errors**

15 In addition to the statistical error, a small systematic error (bias) may affect both water vapour and
16 temperature measurements. For example, for water vapour measurements, besides a bias (not exceed
17 5 %) associated with the estimate of the calibration coefficient (resulting from radiosonde biases,
18 different air masses being sensed by the radiosonde and the lidar), an additional very small bias
19 ($< 1\%$) may be associated with the use of narrowband filters and, consequently, the accurate estimate of
20 the height-dependent correction factor accounting for the temperature dependence of the H_2O and N_2
21 Raman scattering signals selected by these filters, while a 1 % systematic uncertainty may be associated
22 with the determination of the differential transmission term (Whiteman, 2003). For temperature
23 measurements, besides a small bias associated with the estimate of the calibration coefficient, an
24 additional small bias ($< 0.2\text{ K}$) is associated with the assumption of the calibration function (1) to be
25 valid for the selected portions of the rotational Raman spectrum. It is to be pointed out that, as the above
26 mentioned systematic error sources are time independent (see Whiteman, 2003, for water vapour
27 measurements and section 4.2.2 of this paper for temperature measurements), biases can be
28 substantially removed from water vapour and temperature time-series measurements based on the use of
29 suitable spectral filters before calculating their fluctuations; consequently, time-independent systematic
30 errors have a marginal influence on the accuracy of turbulence profiles, especially for a high accuracy
31 system as ours (see equations A1-A8 in Wulfmeyer *et al.*, 2016).

32

2.3.2 Elastic signal ~~cross-talk into~~leakage in the rotational Raman signals and approach for its removal

Specific check and sensitivity studies have been performed in order to verify the presence and amplitude of elastic signal ~~cross-talk into~~leakages in the rotational Raman signals and their potential effect on temperature measurements. In this respect it is to be pointed out that in the present system set-up the low- and high-quantum number rotational Raman signals, $P_{LoJ}(z)$ and $P_{HiJ}(z)$, are collected at 354.3 and 352.9 nm, respectively, these wavelengths being very close to the laser emission at 354.7 nm. Consequently, particular care has to be paid in the definition of the spectral specifications of the interference filters used for the selection of $P_{LoJ}(z)$ and $P_{HiJ}(z)$, especially for what concerns their blocking at 354.7 nm. This is particularly true for the Lo-J filter, having a central wavelength just 0.4 nm off the excitation wavelength, while it is less for the Hi-J filter, as its central wavelength is 1.8 nm off the excitation wavelength. The interference filters used in the present system set-up are characterized by a nominal blocking at 354.7 nm of 10^{-6} - 10^{-7} . However, based on measurements carried out in the presence of clouds, we collected experimental evidence that the effective blocking of our Lo-J filter is not better than 10^{-5} . For this motivation, in previous field deployments (among others, the Convective and Orographically-induced Precipitation Study - COPS, Wulfmeyer *et al.*, 2008; Behrendt *et al.*, 2011), a second narrow-band interference filter was put in cascade to the Lo-J filter, this second filter having the same center wavelength and pass-band of the Lo-J filter (this latter being 0.2 nm full width at half maximum), but having a nominal blocking at 354.7 nm of 10^{-3} . The combination of two filters had been successfully applied before at 532 nm, obtaining undisturbed measurements even in clouds (Behrendt and Reichardt, 2000). Just recently, the possibility to achieve sufficient blocking at 354.7 nm with only one filter could also be demonstrated based on recent advances achieved in multi-cavity interference filter technology (Hammann *et al.*, 2015b). The ultimate goal of using two cascading interference filters was to obtain an overall blocking at 354.7 nm of 10^{-8} or better. However, because of the very narrow pass-band of the two cascading filters, a perfect superimposition of their transmission curves was found difficult to achieve. In this respect it is to be specified that a partial superimposition of the transmission curves of the two filters may determine an even narrower pass-band, ultimately compromising the filters' capability to select the rotational lines necessary for the temperature measurements. Additionally, also when a perfect superimposition of the two cascading filters' transmission curves is achieved, the overall center wavelength transmission is significantly reduced (not exceeding 15 %, with the transmission of the Lo-J filter being 30 % and the transmission of the second

1 cascading filter being 50 %); thus, the introduction of the second cascading filter determines an overall
2 reduction of $P_{LoJ}(z)$ by 50 % and a consequent reduction in measurement precision.

3 In order to avoid these drawbacks, in recent field deployments the second cascading filter was remove
4 from the Lo-J channel, fully aware that this would have determined an overall lower blocking at 354.7
5 nm for the Lo-J interference filter and, consequently, a possible cross-talkleakage of the 354.7 nm
6 elastic lidar signal into the Lo-J rotational Raman signal, but also fully aware of the different research
7 efforts, and corresponding literature papers, dedicated to the definition of approaches to identify and
8 remove elastic signal leakages from the rotational Raman signals (Behrendt *et al.*, 2002; Su *et al.*, 2013).
9 These authors demonstrated that elastic signal cross-talkleakage into the Lo-J rotational Raman signals
10 can be completely removed if simultaneous and co-located measurements of the elastic signal are
11 available. Behrendt *et al.* (2002) tested their approach on a rotational Raman lidar operating at 532 nm,
12 while Su *et al.* (2013) applied their approach to a rotational Raman lidar operating at 354.7 nm. At
13 354.7 nm, the approach considers the expression:

$$14 \quad P_{LoJ}(z) = P_{LoJ}^{leak}(z) - k T_F P_{354.7}(z) \quad (5)$$

15 with $P_{LoJ}^{leak}(z)$ being the leaked Lo-J rotational Raman lidar signal, $P_{LoJ}(z)$ being the effective Lo-J
16 rotational Raman lidar signal used for the derivation of temperature profiles, $P_{354.7}(z)$ being the 354.7
17 nm elastic lidar signal, T_F being the transmission of neutral density filters (used to attenuate the elastic
18 signals and avoid signal induced noise effects associated with the low range echoes), and k being the
19 cross-talkleakage factor. Expression (5) specifies that, if the cross-talkleakage factor is known, the
20 effective Lo-J rotational Raman signal can be determined from leaked Lo-J rotational Raman signal by
21 simply subtracting the 354.7 nm elastic lidar signal from the latter.

22 In this respect, it is to be specified that the simultaneity and co-location of the measured Lo-J and 354.7
23 lidar signals is in our case quite a strict requirement, as in fact the signals necessary for the present
24 turbulence studies are acquired with high vertical and temporal resolution. In our system, the
25 simultaneity is guaranteed by the use of two distinct acquisition channels, with a common triggering,
26 included in a single sampling unit. The co-location of the measurements, i.e. the sounding of the same
27 atmospheric air column, is guaranteed by the use of the same large-aperture telescope for the collection
28 of the two signals and the proximity of the two detection channels within the optical layout of system.
29 In this direction, it is also to be specified that the elastic and rotational Raman scattering are stimulated
30 with the same laser wavelength (354.7 nm) and consequently the radiated air column is the same for the
31 two measurement channels.

1 An accurate estimate of the cross-talk leakage factor k is of paramount importance to remove, or at least
 2 minimize, potential systematic errors associated with any residual elastic signal cross-talk into leakage in
 3 the rotational Raman signals. For this purpose, a modified version of the approach defined by Behrendt
 4 *et al.* (2002) was applied. The approach is based on the selection of a measurement period with clouds,
 5 the calculation of $P_{LoJ}(z)$ for different values of k and the selection of the value of k leading to
 6 temperature values inside the cloud best fitting the temperature values from a near-by radiosonde.

7 For this purpose, we selected a 9 min time interval (13:38-13:46 UTC), shortly after the 2-h time period
 8 considered for the turbulence analysis (11:30-13:30 UTC); as a result of this selection, the value of k
 9 determined for this time interval can be effectively used to correct the data in the time interval
 10 considered in the turbulence analysis. The 9 min time interval is characterized by the presence of high-
 11 level clouds (cirrus clouds) extending between 7.9 and 9.8 km, which are not optically thick, with all
 12 measured lidar signals extending above the cloud top. This characteristic makes the selected time
 13 interval particularly suited for the estimate of k . A 9 min time interval was considered in order to
 14 achieve a sufficiently high signal statistics and, consequently, a lower uncertainty in the determination
 15 of the correct value of k based on the above mentioned best fit procedure. Figure 3 shows the vertical
 16 profiles of $P_{LoJ}^{leak}(z)$, $P_{HiJ}(z)$ and $T_F P_{354.7}(z)$ averaged over the 9 min interval. To better illustrate the
 17 proposed approach, in figure 3 we focused our attention to the vertical interval 6-10 km. The elastic
 18 signal $P_{354.7}(z)$ reveals the presence of several layers associated with cirrus clouds between 7.9 and 9.8
 19 km, with a peak at 9.3 km. The figure clearly highlights the elastic signal cross-talk leakage into $P_{LoJ}^{leak}(z)$
 20 in the height region inside the cloud, while no evidence of elastic signal cross-talk leakage is present in
 21 $P_{HiJ}(z)$ in this same height region. To apply the best fit procedure the radiosonde launched at 13:00
 22 UTC from the near-by launching station in Hambach (approx. 4 km E-SE) was considered. Considering
 23 an ascent speed of 3.5 m s^{-1} , which is the average speed experienced by the present radiosonde in the
 24 height interval from surface up to 10 km, the radiosonde is expected to cover the 8-10 km height region
 25 in the time interval 13:38-13:46 UTC, which is exactly the time interval considered for the application
 26 of our approach. The value of k leading to temperature values inside the cloud best fitting the
 27 radiosonde temperature values was found to be 0.91. The best fit procedure considers all data points
 28 (approx. 70 points) within the height range where the cirrus cloud is located (7.9 and 9.8 km). This
 29 computation was repeated at different times during the cirrus clouds appearance period (12:22-18:52
 30 UTC), also considering the data from the additional radiosondes available in this period (i.e. at 15:00
 31 and 17:00 UTC). Results reveal that k has a constant value of 0.91, with very limited dispersion (0.01)
 32 around this value, i.e. $k \pm \Delta k = 0.91 \pm 0.01$ (Nocera, 2016). This result demonstrates that laser frequency or

1 filter's position fluctuations, potentially generable by thermal drifts inside the laser cavity or the filter's
 2 housing, respectively, have negligible effects on k .

3 It is to be pointed out that **cross-talkleakage** correction increases the statistical uncertainty affecting the
 4 temperature measurement as a result of the subtraction of $P_{354.7}(z)$, which is affected by statistical noise,
 5 from $P_{LoJ}^{leak}(z)$, also affected by statistical noise, the two statistical noises being uncorrelated.
 6 Additionally, the correction factor k is determined with a certain degree of uncertainty (small, but not
 7 negligible), which may lead to a residual systematic error (bias) affecting temperature measurements
 8 after the application of the **cross-talkleakage** correction approach. The systematic error associated with
 9 this residual **cross-talkleakage** may be estimated through error propagation, considering the expression
 10 for $T(z)$ including **cross-talkleakage** correction:

$$11 \quad T(z) = \frac{\alpha}{\ln \left[\frac{P_{HiJ}(z)}{P_{LoJ}^{leak}(z) - k T_F P_{354.7}(z)} \right] - \beta} \quad (6)$$

12 with T_F being the overall transmission ($\sim 10^{-3}$) of the two neutral density filters located in front of the
 13 354.7 nm interference filter. Consequently, the systematic error affecting each temperature profile
 14 associated with the uncertainty affecting k reads:

$$15 \quad \Delta T_{leak}(z) = -\frac{T^2(z)}{\alpha} \frac{k T_F P_{354.7}(z)}{P_{LoJ}^{leak}(z) - k T_F P_{354.7}(z)} \frac{\Delta k}{k} \cong -\frac{T^2(z)}{\alpha} \frac{k T_F P_{354.7}(z)}{P_{LoJ}^{leak}(z)} \frac{\Delta k}{k} = -\frac{T^2(z)}{\alpha} \frac{T_F P_{354.7}(z)}{P_{LoJ}^{leak}(z)} \Delta k \quad (7)$$

16 with Δk being the uncertainty affecting the estimate of k . The **cross-talkleakage** signal is $k T_F P_{354.7}(z)$,
 17 which corresponds to about 22 % of $P_{LoJ}^{leak}(z)$ around the ABL top. Thus, the remaining error affecting
 18 temperature measurements becomes a fluctuating error, which is dependent on atmospheric properties,
 19 mainly on aerosol backscatter contribution to $P_{354.7}(z)$. This effect has to be properly taken into account
 20 in the determination of turbulence profiles, as in fact fluctuations in aerosol particle backscatter,
 21 especially in the upper portion of the CBL, may produce a time-dependent residual systematic error,
 22 which would propagate into the temperature fluctuations. Because of this, the quantity
 23 $P_{LoJ}(z) = P_{LoJ}^{leak}(z) - k T_F P_{354.7}(z)$ has to be properly assessed in expression (6) for each 10 s temperature
 24 profile.

25 Considering an uncertainty of 0.01 on the estimate of k , a value of $T=280$ K, a value of $\alpha=1200$ K
 26 (which is the one resulting from the application of the calibration procedure), the systematic error

1 $\Delta T_{leak}(z)$ associated with residual **cross-talk leakage** in the upper portion of the CBL results to be equal to
 2 0.16 K.

3 An additional overall, spurious term $\overline{(T'_{ov,leak}(z))^2}$ has to be considered in the temperature variance, which
 4 is associated with the residual systematic error affecting temperature measurements after the application
 5 of the **cross-talk leakage** correction approach. This additional contribution is given by:

$$6 \quad \overline{(T'_{ov,leak}(z))^2} \approx \overline{\Delta T'_{leak}{}^2} + 2\overline{T'_{tr}(t)\Delta T'_{leak}(t)} < \overline{\Delta T'_{leak}{}^2} + 2\sqrt{\overline{\Delta T'_{leak}{}^2}}\sqrt{\overline{T'_{tr}{}^2}} \quad (8)$$

7 where the first term in the contribution to the “**cross-talk leakage** variance” due to additional fluctuations
 8 caused by insufficient **cross-talk leakage** correction and the second term is due to the correlation of the
 9 atmospheric temperature fluctuations within the not perfectly corrected **cross-talk leakage**. We find that:

$$10 \quad \overline{\Delta T'_{leak}{}^2} \cong \left[\frac{T^2}{\alpha} \right]^2 \frac{(k T_F)^2 (\overline{P_{354.7}(t)} - \overline{P_{354.7}})^2}{(\overline{P_{LoJ}^{leak}} - k T_F \overline{P_{354.7}})^2} \left(\frac{\Delta k}{k} \right)^2 = \left[\frac{T^2}{\alpha} \right]^2 \frac{(k T_F \overline{P_{354.7}})^2}{(\overline{P_{LoJ}^{leak}} - k T_F \overline{P_{354.7}})^2} \left(\frac{\Delta k}{k} \right)^2 \frac{(\overline{P_{354.7}(t)} - \overline{P_{354.7}})^2}{\overline{P_{354.7}}^2}$$

$$= (\Delta T_{leak})^2 \frac{(\overline{P_{354.7}(t)} - \overline{P_{354.7}})^2}{\overline{P_{354.7}}^2} = (\Delta T_{leak})^2 \frac{\text{var}(\overline{P_{354.7}})}{\overline{P_{354.7}}^2} \approx (0.18\text{K})^2 \frac{1.7 \cdot 10^4}{500^2} = 2.2 \cdot 10^{-3} \text{K}^2 \quad (9)$$

11 where we took the relative variance of the backscatter signal from our data at the ABL top. Here, the
 12 variance is maximum so that we reach an upper limit of the spurious temperature variance of
 13 $2.2 \cdot 10^{-3} \text{K}^2$ which can be neglected with respect to the atmospheric temperature variance (see section
 14 4.3). For the correlation term, however, we get

$$15 \quad \overline{2T'_{tr}(t)\Delta T'_{leak}(t)} < 2\sqrt{\overline{\Delta T'_{leak}{}^2}}\sqrt{\overline{T'_{tr}{}^2}} \approx 2 \cdot 0.048\text{K} \cdot 0.64\text{K} = 0.06\text{K}^2 \quad (10)$$

16 where we took the maximum of the atmospheric temperature variance at the ABL top. This error is still
 17 considerably smaller than our estimate of the atmospheric temperature variance at the peak in the
 18 entrainment layer so that the structures in the higher-order moments are significant.

19 Based on the above considerations, we have to be aware that, besides a random error, represented in
 20 figure 6b with the error bar, an additional systematic error (with a maximum amplitude of 0.16 K)
 21 resulting from residual elastic signal **cross-talk into leakage in** the rotational Raman signals has to be
 22 considered. This is also true when considering the noise error estimated in figure 1c. The missed
 23 inclusion of this systematic error both in figure 6b and figure 1c is due to the very small amplitude of
 24 this contribution; additionally, random and systematic error sources have always to be treated separately
 25 and cannot be just summed up. Additionally, the spurious temperature variance, even if small with
 26 respect to the atmospheric temperature variance, it is always positive. So an iteration with different

1 values for k can also be used to verify the correctness of the above determined value of k , as in fact the
2 correct value minimizes the overall variance.

3 Based on the above mentioned approach, before proceeding with the turbulence analysis, we corrected
4 all 10 sec Lo-J signals for the systematic effect associated with elastic signal cross-talk leakage.
5 However, in order to overcome the residual systematic uncertainty associated with this correction, a
6 future upgrade of *BASIL* is planned with the introduction of a new Lo-J filter, with high blocking at
7 354.7 nm and high center wavelength transmission, to be developed benefiting from the recent advances
8 in multi-cavity interference filter technology.

9

10 **3 Time-height cross-sections of water vapour mixing ratio and temperature**

11 **3.1 Case study and weather conditions**

12 In this paper we illustrate measurements carried out in the framework of the HD(CP)2 Observational
13 Prototype Experiment (HOPE). HOPE, embedded in the project High-Definition Clouds and
14 Precipitation for advancing Climate Prediction (HD(CP)2) of the German Research Ministry, was
15 specifically designed to provide a dataset for the evaluation of the German non-hydrostatic General
16 Circulation Model ICON at the scale of the model simulations. It took place in Western Germany in the
17 time period April-May 2013. For the purposes of HOPE, *BASIL* was deployed in the Supersite JOYCE,
18 located within the Jülich Research Center (Central Germany, Lat.: 50°54' N; Long.: 6°24' E, Elev. 105
19 m). The system operated between 25 March and 31 May 2013, collecting more than 430 hours of
20 measurements distributed over 44 days and 18 IOPs. Quick-looks of these dataset are present on the
21 HOPE Website (<https://code.zmaw.de/projects/hdcp2-obs/>), while water vapour and particle backscatter
22 data can be downloaded from the HD(CP)2 database.

23 In the selection of the case study considered in this paper, attention was paid on identifying weather
24 conditions characterized by the presence of a well-mixed and quasi-stationary CBL. Consequently, in
25 those cases when measurements of the complete CBL cycle are available, i.e. from the onset to its
26 progressive built up and final decay, attention has been focused only on those time segments
27 characterized by a stable or almost stable CBL height, which corresponds to the period of its maximum
28 development. Typically time segments with a duration of 1-2 hours are considered as in fact for longer
29 periods the CBL can no longer be considered as being quasi-stationary, while the consideration of
30 shorter periods would reduce the number of sampled thermals and thus increase the sampling errors.

1 The synoptic condition on 20 April 2013 was characterized by the presence of a high pressure system
2 located over Great Britain, with effects extending over Central-Northern Germany, and a low pressure
3 system located over Central Italy (see also Muppa *et al.*, 2016). The forecast for the HOPE region
4 indicated some thin convective clouds from 8 to 10 UTC and clear sky starting from 10 UTC, with
5 cirrus clouds starting from 15 UTC. This was considered as a day with suitable atmospheric conditions
6 for an Intensive Observation Period (IOP), specifically IOP 5, dedicated to radiometer tomography.
7 This IOP turned out to be also a good case study for the purpose of studying CBL development under
8 clear-sky or almost-clear sky conditions. Indeed, the almost undisturbed solar irradiance resulted in the
9 development of a well-mixed CBL which was not affected by clouds.

11 3.2 Water vapour mixing ratio, temperature, and backscatter fields

12 In order to select an appropriate time interval for the application of the turbulence analysis, we
13 considered the measurements of the different energy balance components as provided by the surface
14 energy balance station in Hambach (not illustrated here). The maximum net radiation was found to
15 occur around 12:00 UTC (520 Wm^{-2}), with a very limited variability ($<40 \text{ Wm}^{-2}$) within the time
16 interval 11:30-13:30 UTC. This is the time interval that we selected for the turbulence analysis.

17 In order to achieve a sufficiently high signal-to-noise error (SNR) and consequently an acceptably low
18 noise error level, a running average over 3 points was considered for the water vapour mixing ratio data,
19 which translates into a reduced vertical resolution of 90 m, while no average was applied to the
20 temperature data, keeping the original vertical resolution of 30 m.

21 Figure 4 illustrates the time-height plot of the particle backscatter coefficient at 1064 nm, β_{par} , between
22 11:30 and 13:30 UTC on 20 April 2014. The figure reveals the presence of a significant aerosol loading
23 within the boundary layer (with values of β_{par} in the range 0.3-1.4 excess of $1 \times 10^{-6} \text{ m}^{-1} \text{ sr}^{-1}$), tracing the
24 presence of a well-mixed and quasi-stationary CBL at this time of the day, extending up to a height of
25 approximately 1300 m. The figure also reveals the presence of alternating updrafts and downdrafts. β_{par}
26 was determined based on the application of a Klett-modified approach (Di Girolamo *et al.*, 1995, 1999).
27 The identification of the CBL height and the monitoring of its variability is made possible by exploiting
28 aerosols² property to act as atmospheric tracers. The mean CBL height, z_i , is an important scaling
29 variable for turbulence profiles. The evolution of the instantaneous CBL height z'_i (black dots in figure
30 4) was determined through the application of a conventional approach based on the detection of the
31 strongest gradient of in the aerosol backscatter signal (see, among others, Pal *et al.*, 2010; Haeffelin *et*
32 *al.*, 2012; Milroy *et al.*, 2012; Summa *et al.*, 2013). Within the considered time interval z'_i is found to be

1 characterized by a limited variability, with a mean value z_i of 1290 m a.g.l and a standard deviation of
2 | 757 m. The minimum and maximum values of z_i during the observation period are 1140 and 1440 m
3 a.g.l., respectively. This result is in very good agreement with the simultaneous measurements
4 performed by the University of Hohenheim Differential Absorption Lidar (UHOH-DIAL) (Wagner *et*
5 *al.*, 2013; Späth *et al.* 2016), deployed in Hambach, approx. 4 km E-SE, with a mean value of 1295 m
6 and a standard deviation of 86 m (Muppa *et al.*, 2016). z_i is used in the remaining part of the paper to
7 determine the normalized height scale z/z_i . Particle backscatter coefficient data can also be used to
8 identify the presence of aerosol layers and/or clouds within and above the CBL, with an effective
9 demonstrated capability to detect cloud bases and tops (the latter in the case of cloud optical thickness
10 typically smaller than 2, Di Girolamo *et al.*, 2009b).

11 Figure 5 illustrates the time-height cross section of water vapour mixing ratio (figure 5a) and
12 temperature (figure 5b) for the same time interval considered in figure 4. Figures 5a and 5b clearly
13 highlights the large variability of water vapour mixing ratio and temperature within the CBL associated
14 with the presence of alternating updrafts and downdrafts. The largest variability of both water vapour
15 mixing ratio and temperature is observed in the interfacial layer, as a result of the penetration of the
16 warm humid air rising from the ground and the entrainment of cool dry air from the free troposphere.
17 Figure 5b also reveals the presence of decreasing temperatures within the CBL up to a minimum around
18 1200-1300 m and an appreciable temperature inversion (approx. 1 K) above.

19 Figure 6 illustrates the mean profile for water vapour mixing ratio (figure 6a) and temperature (figure
20 6b) as measured by *BASIL* over the same time interval considered in figure 4 (11:30-13:30 UTC on 20
21 April 2013), together with the corresponding profiles measured by the radiosonde launched at 13:00
22 UTC from the nearby site of Hambach. The water vapour mixing ratio profiles from *BASIL* and the
23 radiosonde are found to agree within 0.2 g kg^{-1} within the mixed layer. A larger deviation is found in the
24 interfacial layer (0.5 g kg^{-1}). However, this is not surprising when considering that the Raman lidar data
25 are averaged over a 2 h period (11:30-13:30 UTC), while the radiosonde reaches the CBL top few
26 minutes after launch. Besides the different time interval considered for *BASIL* and the radiosonde, the
27 two sensors are also sounding different air masses as a result of the 4 km distance between the lidar site
28 and the radiosonde launching station and the horizontal drift of the sonde during its ascent caused by the
29 wind and the consequent deviation of its atmospheric path from the vertical. In presence of intense
30 convective activity, deviations from the sounding data are also possible for radiosondes launched from
31 the lidar site: in this case humid air updrafts and dry air downdraft may have sizes of few kilometres and
32 consequently the radiosonde data can capture different features during its ascent within the CBL with
33 | respect to the lidar. This property makes lidar systems much more suitable for studying turbulence

1 statistics than in-situ sounding systems. In fact, because of the capability of the formers to monitor the
 2 vertical air column above the station as opposed to radiosondes, undergoing a horizontal drift during
 3 their ascent and consequently a deviation from the vertical, lidar systems guarantee the capability to
 4 measure turbulence statistics within the turbulent eddies involved in the boundary layer mixing
 5 processes. This property makes lidar systems much more suitable for studying turbulence statistics than
 6 in-situ sounding systems as in fact with lidars statistics is indeed measured in a vertical column. Similar
 7 considerations apply for the comparison between *BASIL* and the radiosonde in terms of temperature
 8 profile (figure 6b). In this case, the deviation between the two sensors is $\cong 0.5$ K throughout the CBL,
 9 with *BASIL* being characterized by systematically smaller values than the radiosonde, while a better
 10 agreement (deviation not exceeding 0.3 K) is observed in the free troposphere above the CBL top. In
 11 this respect, it is to be noticed that the sequence of consecutive radiosondes launched during IOP 5 (at
 12 09:00, 11:00, 13:00 UTC, not shown here) reveals the occurrence of vertical profiles characterized by
 13 an almost constant potential temperature values within the mixed layer, as expected for a well-mixed
 14 CBL, with potential temperature constant value progressively increasing with time. Considering that
 15 Raman lidar data in figure 6 are averaged over a 2 h period (11:30-13:30 UTC) which is largely
 16 anticipating the radiosonde launch time (at 13:00 UTC), the systematically smaller temperature values
 17 of *BASIL* with respect to the radiosonde within the CBL are easily justifiable.

19 **4 Turbulence analysis methodology and results**

20 **4.1 Methodology**

21 In CBL turbulence studies, the instantaneous value of a measured atmospheric variable, $x(z,t)$, at height
 22 z , can be expressed as the sum of three terms: a slowly varying or even constant term, $\overline{x(z)}$, where the
 23 over-bar represents the time average over the considered temporal interval for the turbulence analysis, a
 24 fluctuation or perturbation term, $x'(z,t)$ and a system noise term, $\varepsilon(z,t)$, following the expression:

$$25 \quad x(z,t) = \overline{x(z)} + x'(z,t) + \varepsilon(z,t) \quad (11)$$

26 $\overline{x(z)}$ can be derived from applying a linear fit to the data over the time period when the turbulent
 27 processes are studied (typically 60-120 min, 120 min in our case).

28 Here the fluctuation term $x'(z,t)$ represents the de-trended fluctuation term with zero mean. To de-trend
 29 the data within a CBL in quasi-stationary state a linear fit is applied to the atmospheric variable time
 30 series.

1 For any measured atmospheric variable, as atmospheric variance and the noise variance are uncorrelated,
2 total variance can be expressed as (Lenschow *et al.*, 2000):

$$3 \quad \overline{(x'_m(z))^2} = \overline{(x'_a(z))^2} + \overline{(x'_n(z))^2} \quad (12)$$

4 with $\overline{(x'_m(z))^2}$ being the total measured variance, $\overline{(x'_a(z))^2}$ being the atmospheric variance and
5 $\overline{(x'_n(z))^2}$ being the noise variance.

6 Different procedures may be considered to separate atmospheric variance from noise variance in the
7 total measured variance. The auto-covariance method is probably the most effective and straightforward
8 among these procedures. This method is based on the consideration that atmospheric fluctuations are
9 correlated in time, while instrumental noise fluctuations are uncorrelated (Lenschow *et al.*, 2000). This
10 approach allows to determine atmospheric variance based on the computation of the auto-covariance
11 function (ACF) for the considered atmospheric variable and then extrapolating this function to zero lag
12 based on the application of a power-law fit. As specified in Lenschow *et al.* (2000), the auto-covariance
13 function at zero lag represents the total measured variance and, consequently, the noise variance can be
14 determined as the difference between the auto-covariance function extrapolated to zero lag and its value
15 at zero lag.

16 An alternative approach is represented by the spectral method. In this case, the power spectrum of the
17 atmospheric variable fluctuations is computed and the constant white noise level close to the Nyquist
18 frequency is evaluated. Both the spectral method, based on the assumption that the system noise is
19 white, and the auto-covariance method allow to verify whether the major part of the turbulent
20 fluctuations is resolved through the measurements either by comparing the high-frequency component
21 of the spectrum with the theoretical decay in the inertial sub-range or by fitting the turbulent structure
22 function to the auto-covariance function. Thus, there is no reason to transfer the data in the spectral
23 domain for these applications and, because of that, the data analysis was kept in the time domain.
24 Furthermore, while both approaches were considered and tested on the water vapour and temperature
25 data considered in this paper, the auto-covariance technique (see figure 1) is to be preferred because of
26 its capability to directly determine system noise variance by means of the Fourier transformation of the
27 auto-covariance function, without introducing additional uncertainties (Wulfmeyer *et al.*, 2010).

28 Preliminary pre-processing steps have to be applied to the data before both techniques can be applied. In
29 general, before any further processing, spikes must be detected and flagged, as they negatively affect
30 the calculation of turbulent variables (Senff *et al.*, 1996). In fact, the presence of spikes in the time

1 series may have a significant impact on the computations of higher moments of the turbulent statistics.
2 Spikes in water vapour and temperature profiles are primarily resulting from non-linear effects
3 associated with the application of retrieval algorithms, these being likely to happen especially at low
4 signal-to-noise levels (Di Girolamo *et al.*, 2008). Low signal-to-noise levels are typically found in day-
5 time Raman lidar water vapour and temperature measurements at heights above 3-5 km, this height
6 varying depending on the considered variable (being lower for water vapour and higher for temperature),
7 or in the presence of clouds as a result of the laser beam attenuation. For the application considered in
8 this paper, i.e. the characterization of turbulent processes within the CBL, the vertical range of interest
9 is up to 2000 m and within this range the signal-to-noise level of rotational and vibrational Raman
10 signals is typically large enough to refrain from applying the spike removal algorithm to the data.
11 Additionally, for the specific case study considered in this paper, clouds are completely missing within
12 the CBL, and consequently the application of the spike removal algorithm to the lidar data returns a
13 dataset with almost no data removed. However, there may be missing data or data gaps generated in the
14 adaptation of the time resolution; because of this, a spike detection algorithm (McNicholas and Turner,
15 2014) is routinely applied to the data before either the auto-covariance method or the spectral method
16 are applied.

17

18 **4.2 Turbulent fluctuations, corresponding auto-covariance functions and assessment of the noise** 19 **error**

20 Figure 7 illustrates the time-height cross section of water vapour mixing ratio (figure 7a) and
21 temperature fluctuations (figure 7b) in the same time interval considered in figure 4. Positive and
22 negative humidity and temperature fluctuations are present within the CBL. In the interfacial layer, the
23 fluctuations become larger than below. More specifically, instantaneous water vapour fluctuations are
24 within $\pm 0.5 \text{ g kg}^{-1}$ in the mixed layer and $\pm 1 \text{ g kg}^{-1}$ in the interfacial layer, while instantaneous
25 temperature fluctuations are within $\pm 0.5 \text{ K}$ in the mixed layer and $\pm 1 \text{ K}$ in the interfacial layer. In the
26 free troposphere humidity and temperature fluctuations are almost completely missing and the observed
27 variability is primarily driven by instrumental noise.

28 Figure 8 shows the auto-covariance functions obtained from water vapour (figure 8a) and temperature
29 fluctuations (figure 8b) for the height levels between 400 and 1600 m a.g.l., i.e., 0.3 to 1.25 z_i , and for
30 lags from -200 to 200 s. As mentioned earlier, the difference between the peak at zero lag and the first
31 lag provides an estimate of the system noise variance. This is also described in figures 8a and 8b, where
32 the structure functions have been fitted to the auto-covariance functions for the height levels of 1230 m

1 and 1410 m to verify the feasibility and reliability of this approach. In the figure, this difference is
2 found to increase with height for both variables as a result of the increasing system statistical noise.
3 Values of the ACFs close to the zero lag provide an estimate of the atmospheric variance: larger values
4 for the ACFs found in the figure at 1230 and 1410 m indicate a larger atmospheric variance at these
5 heights, as a result of the large atmospheric variability within the interfacial layer.

6

7 **4.3 Measurements of higher-order moments**

8 Figure 9 illustrates the integral scale (IS) of water vapour mixing ratio (figure 9a) and temperature
9 fluctuations (figure 9b) computed for the same time interval considered in figure 4. The integral time
10 scale can be considered as an estimate of the mean size of the turbulent eddies involved in the boundary
11 layer mixing processes. The integral time scale of both water vapour mixing ratio and temperature
12 fluctuations is found to have large values (also [in excess of 200 s, up to 500 s for water vapour](#)) in
13 the lower portion of the CBL up to $\cong 750$ m (i.e. $z/z_i < 0.6$). Values of the integral scale for water vapour
14 mixing ratio fluctuations in the upper portion of the CBL (above 750 m) are in the range 70-125 s, with
15 a peak value of 125 s at 1230 m (i.e. $z/z_i = 0.95$). These values are in agreement with those reported for
16 water vapour by Wulfmeyer *et al.* (2010, 70-130 s) and by Turner *et al.*, 2014a (120-140), as well as
17 with the simultaneous nearby measurements performed by the UHOH-DIAL, with values in the range
18 60-130 s (Muppa *et al.*, 2016). Values of the integral scale for temperature fluctuations in the upper
19 portion of the CBL are in the range 75-225 s, with a peak value of 225 s around the top of the CBL (at
20 1310 m). These values are in agreement with those reported by Behrendt *et al.* (2015, 40-120 s) for the
21 nearby site of Hambach, but a different case study. Values of the integral scale throughout the CBL for
22 both water vapour and temperature fluctuations are much larger than the temporal resolution used for
23 the measurements (10 s), which demonstrates that the considered temporal resolution is high enough to
24 characterize the major part of turbulence inertial sub-range and consequently resolve the major part of
25 the CBL turbulent fluctuations.

26 Figure 10 shows the vertical profiles of atmospheric and total variance for water vapour mixing ratio
27 (panel a) and temperature (panel b), including noise errors. Water vapour mixing ratio variance is
28 almost zero up to $\cong 750$ m (i.e. $z/z_i = 0.6$), it keeps small ($< 0.05 \text{ g}^2\text{kg}^{-2}$) in the middle and upper portion
29 of the CBL ($750 \text{ m} < z < 1100 \text{ m}$, i.e. $0.6 < z/z_i < 0.85$), and it sensitively increases in the interfacial layer
30 due to the entrainment effects. The maximum of the variance profile in the interfacial layer is 0.287
31 g^2kg^{-2} at 1260 m (i.e. $z/z_i = 0.98$), with $0.051 \text{ g}^2\text{kg}^{-2}$ and $0.034 \text{ g}^2\text{kg}^{-2}$ being the sampling error and noise
32 error, respectively. The near-zero values in the lower portion of the CBL are typical and indicate weak

1 forcing from the surface. In the interfacial layer, the variance reaches a maximum as a result of the large
2 water vapour mixing ratio variability which is generated by the vertical exchange associated with the
3 strong updrafts and downdrafts (Wulfmeyer *et al.*, 2010; Turner *et al.* 2014a, Muppa *et al.*, 2016).
4 Variance values at the top of the CBL are in good agreement with those reported by Wulfmeyer
5 (1999a,b, 0.1–0.2 g²kg⁻²), Lenschow *et al.* (2000, 0.1–0.2 g²kg⁻²) and Kiemle *et al.* (1997, 0.3–0.45
6 g²kg⁻²), as well as with the simultaneous nearby measurements by the UHOH-DIAL, with a peak value
7 in the interfacial layer of 0.39 g²m⁻⁶, corresponding to 0.19 g²kg⁻². The full width at half maximum of
8 the largest variability in the entrainment zone is 240 m, i.e. 0.19 z/z_i, in agreement with measurements
9 reported by Wulfmeyer *et al.* (2010, 0.16 z/z_i) and by Turner *et al.* (2014a, 0.15 z/z_i). Values of water
10 vapour mixing ratio variance decrease above the CBL top to approach zero around 1500 m.

11 For what concerns the temperature variance, this keeps smaller than 0.1 K² in the middle and upper
12 portion of the CBL up to 1150 (i.e. z/z_i<0.9). Larger values are observed in the interfacial layer, with a
13 maximum of 0.260 K² at 1310 m (i.e. z/z_i=1.02), with 0.051 K² and 0.035 K² for the sampling error and
14 noise error, respectively. Larger values of the temperature variance in the interfacial layer are the result
15 of the penetration of the warm humid air rising from the ground and the entrainment of cool dry air
16 from the free troposphere (Stull, 1988; Behrendt *et al.*, 2015; Wulfmeyer *et al.*, 2016). Temperature
17 variance decreases above the CBL top to approach zero around 1450 m. The full width at half
18 maximum of the largest variability in the entrainment zone is 240 m, i.e. z/z_i=0.2. Similar peak variance
19 values (0.40 K²) at the top of the CBL were also observed by Behrendt *et al.* (2015) and Wulfmeyer *et al.*
20 *et al.* (2016). It is to be noticed that both water vapour mixing ratio and temperature variance are
21 characterized by very small sampling and noise errors, which make the quality of the present turbulence
22 measurements very high and demonstrates how well the structures present in these profile can be
23 determined.

24 Figure 11 illustrates the vertical profiles of the third-order moment for water vapour mixing ratio (panel
25 a) and temperature (panel b). The third-order moment of a variable quantifies the degree of asymmetry
26 of its distribution, with positive values indicating a right-skewed distribution (with the mode smaller
27 than the mean) and negative values indicating a left-skewed distribution (with the mode larger than the
28 mean). Again, third-order moment estimates are characterized by very small errors, which testify the
29 high quality of the present measurements of this turbulent variable. In figure 11 values of the third order
30 moment of water vapour mixing ratio fluctuations are found to be close to zero between 400 and 900 m
31 (i.e. for 0.3 z_i < z < 0.7 z_i) and are negative between 900 and 1290 m (i.e. for 0.7 z_i < z < z_i), with a
32 negative peak value of -0.029±0.005 g³kg⁻³ at 1140 m. A large positive peak is observed just above
33 CBL top, with a maximum of 0.156±0.009 g³kg⁻³ at 1380 m (z=1.07 z_i).

1 Negative values for the water vapour mixing ratio third-order moment in the upper portion of the CBL
2 is the result of the sharp entrainment of dry air pockets into the boundary layer, which gradually mix
3 with the environmental air (Couvreur *et al.*, 2005, 2007; Wulfmeyer *et al.*, 2010; Turner *et al.*, 2014a,
4 Wulfmeyer *et al.*, 2016). Positive values for the water vapour mixing ratio third-order moment above
5 the top of the CBL are associated with narrow, but strong, convective plumes that penetrate up to this
6 height. The sign and shape of the third-order moment at the top of the boundary layer may also depend
7 on the humidity gradient above the CBL (Couvreur *et al.*, 2007). The near-zero third-order moment
8 values in the mixed layer ($z/z_i < 0.7$) is to be attributed to a symmetric transport process of moisture
9 (Mahrt, 1991; Wulfmeyer *et al.*, 2010).

10 For what concerns the temperature third-order moment, this shows values close to zero ($<0.01 \text{ K}^3$) up to
11 1100 m ($z/z_i < 0.85$) and slightly positive values between 1100 and 1310 m ($0.85 z_i < z < 1.02 z_i$), with
12 a positive peak of 0.055 K^3 at 1220 m. Above 1250 m it becomes negative, with a negative peak of -
13 $0.067 \pm 0.01 \text{ K}^3$ at 1400 m ($z/z_i = 1.1$). The structure of this moment is basically inverted with respect to
14 water vapour (Behrendt *et al.*, 2015). This makes sense because the water vapour gradient is negative in
15 the entrainment zone, whereas the temperature inversion gradient is positive. The positive peak in the
16 interfacial layer is evidence of the predominant effect of narrow warm air downdrafts in the interfacial
17 layer, while the negative peak above the CBL top is the result of narrow cooler updrafts above the CBL
18 top associated with thermals from the surface. Figure 11b, besides temperature third-order moment, also
19 includes the vertical profile of the water vapour mixing ratio third-order moment to better compare the
20 shapes and locations of the peaks and zero crossing values for these two profiles. This allows to reveal
21 that the negative peak in the temperature third-order moment appears at the same height (within 20 m)
22 of the positive peak in the water vapour mixing ratio third-order moment, while the distance between
23 the zero crossing values for the two profiles is approx. 100 m.

24 Figure 12 illustrates the vertical profiles of the fourth-order moment for water vapour mixing ratio
25 (panel a) and temperature (panel b). The fourth-order moment of a variable gives an indication of the
26 steepness of its distribution and the width of its peak. Water vapour mixing ratio fourth-order moment is
27 almost zero up to $\cong 750 \text{ m}$ (i.e. $z/z_i = 0.6$), keeps smaller than $0.02 \text{ g}^4 \text{ kg}^{-4}$ in the middle and upper portion
28 of the CBL ($750 \text{ m} < z < 1100 \text{ m}$, i.e. $0.6 < z/z_i < 0.85$) and increases above 1100 m, reaching its maximum
29 of $0.28 \pm 0.13 \text{ g}^4 \text{ kg}^{-4}$ around the top of the CBL (at 1350 m). It gets again close to zero above 1530 m.
30 Similarly, temperature fourth-order moment is almost zero ($<0.05 \text{ K}^4$) up to 1100 m (i.e. $z/z_i = 0.85$) and
31 has positive values above, reaching a positive peak of $0.24 \pm 0.10 \text{ K}^4$ around the top of the CBL (at 1370
32 m, i.e. $z/z_i = 1.06$). It gets again smaller than 0.05 K^4 above 1500 m (i.e. $z/z_i = 1.15$).

1 Besides the third- and fourth-order moments, also atmospheric skewness and kurtosis has been
2 determined for both water vapour mixing ratio and temperature fluctuations. Figure 13 illustrates the
3 vertical profiles of skewness (panel a) and kurtosis (panel b) for water vapour mixing ratio and
4 temperature. Values of water vapour mixing ratio skewness are in very good agreement with those
5 reported by Wulfmeyer *et al.*, 2010, with positive values (up to 1.5) in the lower portion of the CBL (up
6 to 800 m, i.e. $z/z_i=0.65$), with negative values (down to -1) in the middle and upper portion of the CBL
7 ($800 < z < 1290$ m, i.e. $0.65 < z/z_i < 1.00$). Large and positive values are found within the entrainment zone
8 and just above the PBL-CBL top (with a maximum of approx. 5 at 1400 m, i.e. $z/z_i=1.15$), which
9 testifies the presence of humidity fluctuations strongly deviating from a normal distribution. Values and
10 vertical structure of water vapour mixing ratio skewness are also in good agreement with the
11 simultaneous and nearby measurements performed by the UHOH-DIAL (Muppa *et al.*, 2016), with
12 negative values (down to -1.16) in the middle and upper portion of the CBL ($0.35 < z/z_i < 1.00$) and
13 positive values just above the PBL top (with a maximum of approx. 1 at $z/z_i=1.05$), as well as with the
14 measurements reported by Turner *et al.* (2014), with negative values (down to ~ -1) up to the CBL top,
15 zero values around z_i and positive values just above the CBL top (with a maximum of approx. 1 at z/z_i
16 $=1.1$).

17 Temperature skewness has a negative peak (~ -4) at 500 m, i.e. $z/z_i=0.4$, positive peaks (~ 84 and 48) at
18 890 and 1100 m (i.e. $z/z_i=0.7$ and $z/z_i=0.85$), respectively, and a negative values within the entrainment
19 zone and just above the CBL top (with a peak value of ~ -7) at 1460 m, i.e. $z/z_i=1.13$), in in good
20 agreement with measurements reported by Behrendt *et al.* (2015, 40-120 s) for the nearby site of
21 Hambach, but a different case study. Again, values of skewness within the entrainment zone and just
22 above the CBL top are found to be large, as expected for temperature fluctuations strongly deviating
23 from a normal distribution.

24 Values of kurtosis in the upper portion of the CBL in the entrainment zone (in the height interval 1160-
25 1340-1280 m) are in the range 2.3576-4.333.83, with a mean value of 3.1536, for water vapour mixing
26 ratio fluctuations, while they are in the range 2.68-3.45, with a mean value of 3.172.59-4.11, with a
27 mean value of 3.22, for temperature fluctuations. These values indicate normally distributed
28 (mesokurtic-Gaussian distribution) humidity and temperature fluctuations in the upper portion of the
29 CBL entrainment zone (Wulfmeyer *et al.*, 2010; Turner *et al.* 2014a, Behrendt *et al.*, 2015, Muppa *et al.*,
30 2016). In the entrainment zone and above the CBL top, values of water vapour mixing ratio and
31 temperature kurtosis are found to be large (up to 18) as a result of the presence of humidity and
32 temperature fluctuations strongly deviating from a normal distribution.

1
2
3
4
5
6
7
8
9
10
11
12
13
14
15
16
17
18
19
20
21
22
23
24
25
26
27
28
29
30
31
32

5 Summary

This paper illustrates measurements performed by the Raman lidar system *BASIL* during a recent field deployment which demonstrate the capability of this remote sensor to characterize turbulent processes within the CBL. For the first time simultaneous and co-located daytime measurements of the vertical profiles of higher-order moments of the turbulent fluctuations of water vapour and temperature carried out by a single instrument are reported. Thus, this paper demonstrates that state-of-art lidar systems, with both rotational and vibrational Raman measurement capability, allow for simultaneously determining higher-order moments (as well as skewness and kurtosis) of the fluctuations of these two fundamental turbulent variables. Results are based on the application of the auto-covariance analysis introduced by Lenschow *et al.* (2000) to high-resolution water vapour mixing ratio (10 s, 90 m) and temperature (10 s, 30 m) time series.

Measurements of water vapour turbulent fluctuations throughout the CBL by vibrational Raman lidar, with estimates of up to the fourth-order moment, had been demonstrated to be possible by Wulfmeyer *et al.* (2010) based on the use of the data from the Atmospheric Radiation Measurement (ARM) Raman lidar operated at the Southern Great Plains Climate Research Facility site in Oklahoma (U.S.A.). The same was demonstrated by Behrendt *et al.* (2015) for temperature turbulent fluctuations with rotational Raman lidar. To the best of our knowledge, *BASIL* is the first Raman lidar system demonstrating the capability to simultaneously measure profiles of water vapour and temperature turbulent fluctuations up to the fourth order during daytime throughout the atmospheric CBL.

In the present paper a comprehensive assessment of the performances of the Raman lidar system *BASIL* has been also carried out. Noise error profiles have been estimated based on the application of the auto-covariance method and compared with the noise profiles estimated through Poisson statistics. The measurements of the higher-order moments of water vapour mixing ratio and temperature fluctuations are characterized by very small sampling and noise errors, which make the quality of the present turbulence measurements very high and demonstrates their capability to accurately observe the structures present in the turbulent variables' profiles. In the determination of the temperature profiles, particular care was dedicated in minimizing the potential systematic error associated with elastic signal ~~cross-talk into leakage in~~ the rotational Raman signals. For this purpose, a specific algorithm was illustrated and tested, which allowed to identify and remove signal leakages and to assess the residual systematic uncertainty affecting temperature measurements after correction. In order to overcome the systematic uncertainty associated with this correction, a future upgrade of *BASIL* is planned with the

1 introduction of a new Lo-J filter with high blocking at 354.7 nm and high center wavelength
2 transmission to be developed benefiting from the recent advances in multi-cavity interference filter
3 technology.

4 Limited data is presently available in literature in terms of measurements or model simulations of
5 higher-order moments for both water vapour mixing ratio and temperature fluctuations. Consequently, a
6 deeper insight into possible interpretations of their vertical variability lacks of additional supporting
7 data. The availability of state-of-art rotational and vibrational Raman lidar systems capable to provide
8 high-resolution and accurate water vapour and temperature measurements will certainly help to fill this
9 gap, at least on the measurement side.

10 Future evolutions of this research work include the possibility to (i) compare - for a large variety of
11 clear sky cases collected during HOPE field campaign - the measurements of higher-order moments of
12 moisture and temperature fluctuations performed by *BASIL* with those simultaneously measured by the
13 University of Hohenheim water vapour DIAL and temperature rotational Raman lidar (located approx.
14 4 km E-SE), (ii) extend the analysis to cloud-topped CBLs from different field deployments, as in fact
15 important effect of clouds on turbulent exchange processes in the entrainment zone are expected to be
16 relevant, (iii) compare the measurements of higher-order moments of moisture and temperature
17 fluctuations from *BASIL* with estimates from large eddy simulation, and (iv) complement these studies
18 with a dedicated evaluation of the correlation between temperature and moisture.

19 As a final remark, we need to specify that we foresee the possibility to apply this approach to
20 characterize the diurnal evolution of turbulent processes within the convective boundary layer, by
21 monitoring the changing patterns of water vapour and temperature higher-order moments during its
22 different evolution phases, including day-to-night and night-to-day transitions, possibly with increased
23 temporal resolution. However, measurements of turbulent processes with increased temporal resolution
24 obtained by reducing the time window for the application of the auto-covariance approach to one hour
25 or less would lead to an increase of the sampling error. This can be overcome by the analysis of
26 continuous measurements such as those carried out at observatories like the ARM Southern Great Plains
27 (SGP) site in Oklahoma (USA), the DWD Meteorologisches Observatorium in Lindenberg (Germany)
28 and the Meteo-Swiss Centre for Meteorological Measurement Technology in Payerne (Switzerland).
29 Furthermore, more data will become available via new field campaigns. An example for a pioneering
30 campaign applying these techniques is the forthcoming Land-Atmosphere Feedback Experiment (LAFE,
31 Wulfmeyer and Turner, 2016) to be held at the SGP site (see www.arm.gov/publications/programdocs/

1 [doe-sc-arm-16-038.pdf](#)). Finally, in order to apply the auto-covariance approach to characterize the
2 diurnal evolution of turbulent processes in clear sky conditions, as well as in more complex
3 meteorological situations, i.e in the presence of large-scale advection, synoptic processes and cloud-
4 topped convective boundary layer, modifications in the de-trending approach considered in the present
5 paper are required.

7 **Acknowledgments**

8 Measurements illustrated in this paper were supported on the basis of a specific cooperation agreement
9 between Scuola di Ingegneria - Università degli Studi della Basilicata, Leibniz Institute for
10 Tropospheric Research and Max Planck Institute. We also wish to thank Dr. Dario Stelitano, from
11 Scuola di Ingegneria - Università degli Studi della Basilicata, and Dr. Eva Hammann, from the Institut
12 für Physik und Meteorologie, Universität Hohenheim, for their support in the collection and analysis of
13 the present data set.

15 **References**

- 16 Behrendt, A., and J. Reichardt: Atmospheric temperature profiling in the presence of clouds with a pure
17 rotational Raman lidar by use of an interference-filter-based polychromator, *Appl. Opt.*, 39, 9, p. 1372-
18 1378, doi: 10.1364/AO.39.001372, 2000.
- 19 Behrendt, A., Nakamura, T., Onishi, M., Baumgart, R., and Tsuda, T.: Combined Raman lidar for the
20 measurement of atmospheric temperature, water vapor, particle extinction coefficient, and particle
21 backscatter coefficient, *Appl. Optics*, 41, 7657–7666, doi: 10.1364/AO.41.007657, 2002.
- 22 Behrendt, A.: Temperature Measurements with Lidar. In: C. Weitkamp (Ed.), *Lidar: Range-Resolved
23 Optical Remote Sensing of the Atmosphere*, Springer Series in Optical Sciences, Vol. 102, ISBN: 0-
24 387-40075-3, Springer, New York, 273-305, doi: 10.1007/0-387-25101-4_10, 2005.
- 25 Behrendt, A., Pal, S., Aoshima, F., Bender, M., Blyth, A., Corsmeier, U., Cuesta, J., Dick, G.,
26 Dorninger, M., Flamant, C., Di Girolamo, P., Gorgar, T., Huang, Y., Kalthoff, N., Khodayar, S.,
27 Mannstein, H., Träumner, K., Wieser, A., and Wulfmeyer, V.: Observations of convection initiation
28 processes with a suite of state-of-the-art research instruments during COPS IOP8b, *Q. J. Roy. Meteor.
29 Soc.*, 137, 81–100, doi: 10.1002/qj.758, 2011a.
- 30 Behrendt, A., Pal, S., Wulfmeyer, V., Valdebenito B., Á. M., and Lammel, G.: A novel approach for the
31 char-acterisation of transport and optical properties of aerosol particles near sources, Part I:

1 measurement of particle backscatter coefficient maps with a scanning UV lidar, *Atmos. Environ.*, 45,
2 2795–2802, doi:10.1016/j.atmosenv.2011.02.061, 2011b.

3 Behrendt, A., Wulfmeyer, V., Hammann, E., Muppa, S. K., and Pal, S.: Profiles of second to third order
4 moments of turbulent temperature fluctuations in the convective boundary layer: First measurements
5 with rotational Raman lidar, *Atmos. Chem. Phys.*, 15, 5485–5500, DOI:10.5194/acp-15-5485-2015,
6 2015.

7 Bengtsson, L., Hodges, K. I., and Hagemann, S.: Sensitivity of the ERA40 reanalysis to the observing
8 system: determination of the global atmospheric circulation from reduced observations, *Tellus A*, 56,
9 456–471, doi:10.1111/j.1600-0870.2004.00079.x, 2004.

10 Berg, L. K., Stull, R. B.: A simple parameterization coupling the convective daytime boundary layer
11 and fair-weather cumuli, *J. Atmos. Sci.*, 62, 1976–1988, DOI: <http://dx.doi.org/10.1175/JAS3437.1>,
12 2005.

13 Bhawar, R., Di Girolamo, P., Summa, D., Flamant, C., Althausen, D., Behrendt, A., Kiemle, C., Bossler,
14 P., Cacciani, M., Champollion, C., Di Iorio, T., Engelmann, R., Herold, C., Pal, S., Riede, A., Wirth, M.,
15 and Wulfmeyer, V.: The Water vapour intercomparison effort in the framework of the convective and
16 orographically-induced precipitation study: air-borne-to-ground-based and airborne-to-airborne lidar
17 systems, *COPS Special Issue, Q. J. Roy. Meteor. Soc.*, 137, 325–348, doi: 10.1002/qj.697, 2011.

18 Couvreux, F., Guichard, F., Redelsperger, J-L., Kiemle, C., Masson, V., Lafore, J-P., Flamant, C.:
19 Water-vapour velocity within a convective boundary layer assessed by large-eddy simulations and
20 IHOP_2002 observations. *Q. J. Roy. Meteor. Soc.*, 131, 2665–2693, doi: 10.1256/qj.04.167, 2005.

21 Couvreux, F., Guichard, F., Masson, V., Redelsperger, J-L. : Negative water-vapour skewness and dry
22 tongues in the convective boundary layer: observations and large-eddy simulation budget analysis.
23 *Boundary-Layer Meteorol.*, 123, 269–294, doi:10.1007/s10546-006-9140-y, 2007.

24 Dierer, S., Arpagaus, M., Seifert, A., Avgoustoglou, E., Dumitrache, R., Grazzini, F., Mercogliano, P.,
25 Milelli, M., and Starosta, K.: Deficiencies in quantitative precipitation forecasts: sensitivity studies
26 using the COSMO model, *Meteorol. Z.*, 18, 631–645, doi:10.1127/0941-2948/2009/0420, 2009.

27 Di Girolamo, P., R. V. Gagliardi, G. Pappalardo, N. Spinelli, R. Velotta, V. Berardi: Two wavelength
28 Lidar analysis of stratospheric aerosol size distribution, *J. Aerosol Sci.*, 26, 989–1001, ISSN: 0021-8502,
29 doi: 10.1016/0021-8502(95)00025-8, 1995.

- 1 Di Girolamo, P., P. F. Ambrico, A. Amodeo, A. Boselli, G. Pappalardo, N. Spinelli: Aerosol
2 observations by Lidar in the Nocturnal Boundary Layer, *App. Opt.*, 38, 4585-4595, ISSN: 0003-6935,
3 doi: 10.1364/AO.38.004585, 1999.
- 4 Di Girolamo, P., Marchese, R., Whiteman, D. N., Demoz B. B.: Rotational Raman Lidar measurements
5 of atmospheric temperature in the UV. *Geophys. Res. Lett.*, 31, L01106, ISSN: 0094-8276, doi:
6 10.1029/2003GL018342, 2004.
- 7 Di Girolamo, P., Behrendt, A., and Wulfmeyer, V.: Spaceborne profiling of atmospheric temperature
8 and particle extinction with pure rotational Raman Lidar and of relative humidity in combination with
9 differential absorption Lidar: performance simulations. *Appl. Opt.*, 45, 2474-2494, doi:
10 10.1364/AO.45.002474, 2006.
- 11 Di Girolamo, P., Behrendt, A., Kiemle, C., Wulfmeyer, V., Bauer, H., Summa, D., Dornbrack, A., Ehret,
12 G.: Simulation of satellite water vapour lidar measurements: Performance assessment under real
13 atmospheric conditions. *Rem. Sens. Environ.*, 112, 1552-1568, doi: 10.1016/j.rse.2007.08.008, 2008.
- 14 Di Girolamo, P., Summa, D., Ferretti, R.: Multiparameter Raman Lidar Measurements for the
15 Characterization of a Dry Stratospheric Intrusion Event. *J. Atm. Ocean. Tech.*, 26, 1742-1762, doi:
16 10.1175/2009JTECHA1253.1, 2009a.
- 17 Di Girolamo, P., D. Summa, R. F. Lin, T. Maestri, R. Rizzi, G. Masiello: UV Raman lidar
18 measurements of relative humidity for the characterization of cirrus cloud microphysical properties,
19 *Atmos. Chem. Phys.*, 9, 8799-8811, 2009b. doi:10.5194/acp-9-8799-2009, 2009b.
- 20 Di Girolamo, P., D. Summa, R. Bhawar, T. Di Iorio, M. Cacciani, I. Veselovskii, O. Dubovik, A.
21 Kolgotin: Raman lidar observations of a Saharan dust outbreak event: Characterization of the dust
22 optical properties and determination of particle size and microphysical parameters, *Atmos. Envir.*, 50,
23 66-78, 2012a. doi: 10.1016/j.atmosenv.2011.12.061, 2012a.
- 24 Di Girolamo, P., D. Summa, M. Cacciani, E. G. Norton, G. Peters, Y. Dufournet: Lidar and radar
25 measurements of the melting layer: observations of dark and bright band phenomena, *Atmos. Chem.*
26 *Phys.*, 12, 4143-4157, 2012b. doi: 10.5194/acp-12-4143-2012, 2012b.
- 27 Di Girolamo, P., C. Flamant, M. Cacciani, E. Richard, V. Ducrocq, D. Summa, D. Stelitano, N. Fourrié
28 and F. Saïd, Observation of low-level wind reversals in the Gulf of Lion area and their impact on the
29 water vapour variability, *Q. J. Roy. Meteor. Soc.*, doi: 10.1002/qj.2767, 2016a.
- 30 Di Girolamo, P., Cacciani, D., Scoccione, A., Summa, D., Turner, D. D., Wulfmeyer, V., Schween, J.
31 H., Crewell, S.: Deployment of the of the Raman lidar system BASIL in the frame of the HD(CP)2

1 Observational Prototype Experiment – HOPE: upgrades of the instrument to fulfil the aims of the
2 experiment and overview of the performed measurements, in preparation, to be submitted for
3 publication in *Atmos. Chem. Phys.*, 2016b.

4 Eberhard, W. L., Cupp, R. E., Healy, K. R.: Doppler lidar measurement of profiles of turbulence and
5 momentum flux. *J. Atm. Ocean. Tech.*, 6, 809–819, DOI: [http://dx.doi.org/10.1175/1520-
6 0426\(1989\)006<0809:DLMOPO>2.0.CO;2](http://dx.doi.org/10.1175/1520-0426(1989)006<0809:DLMOPO>2.0.CO;2), 1989.

7 Frehlich, R., and Cornman, L.: Estimating spatial velocity statistics with coherent Doppler lidar. *J. Atm.*
8 *Ocean. Tech.*, 19, 355–366, DOI: <http://dx.doi.org/10.1175/1520-0426-19.3.355>, 2002.

9 Garratt, J. R.: *The Atmospheric Boundary Layer*, Cambridge Atmospheric and Space Science Series,
10 pages 336, ISBN: 9780521467452, 1992.

11 Griaznov, V., I. Veselovskii, P. Di Girolamo, M. Korenskii, D. Summa: Spatial distribution of doubly
12 scattered polarized laser radiation in the focal plane of a lidar receiver, *Appl. Opt.*, 46, 6821–6830, doi:
13 [10.1364/AO.46.006821](https://doi.org/10.1364/AO.46.006821), 2007.

14 Gustafson, W. I. Jr, and Berg, L. K.: Implementation of the probabilistic CuP cumulus parameterization
15 in WRF. In: 8th annual WRF user’s workshop, Boulder, USA, June 11–15, 2007.

16 [Haeffelin, M., Angelini, F., Morille, Y., Martucci, G., Frey, S., Gobbi, G. P., Lolli S., O’Dowd L. C. D.,
17 Sauvage, L., Xueref-Rémy, I., Wastine, B., Feist, D. G.: Evaluation of Mixing-Height Retrievals from
18 Automatic Profiling Lidars and Ceilometers in View of Future Integrated Networks in Europe,
19 *Boundary-Layer Meteorol.*, 143, 49-75, doi:10.1007/s10546-011-9643-z, 2012.](#)

20 Hammann, E., Behrendt, A., Le Mounier, F., and Wulfmeyer, V.: Temperature profiling of the
21 atmospheric boundary layer with rotational raman lidar during the HD(CP)2 5 observational prototype
22 experiment, *Atmos. Chem. Phys.*, 15, 2867-2881, doi:10.5194/acp-15-2867-2015, 2015a.

23 Hammann, E., A. Behrendt, V. Wulfmeyer: Recent upgrades of the rotational Raman lidar of the
24 University of Hohenheim for the measurement of temperature profiles in the surface layer. Reviewed
25 extended abstracts of the 27th International Laser Radar Conference (ILRC27), paper #249, New York
26 City, USA, July 5 - 10, 2015b.

27 Kalthoff, N., M. Kohler, C. Barthlott, B. Adler, S. D. Mobbs, U. Corsmeier, K. Träumner, T. Foken, R.
28 Eigenmann, L. Krauss, S. Khodayar, P. Di Girolamo: The dependence of convection-related parameters
29 on surface and boundary-layer conditions over complex terrain. *Q. J. Roy. Meteor. Soc.*, 137, 70-80,
30 ISSN: 0035-9009, doi: [10.1002/qj.686](https://doi.org/10.1002/qj.686), 2011.

1 Kiemle, C., Ehret, G., Giez, A., Davis, K. J., Lenschow, D. H., and Oncley, S. P.: Estimation of
2 boundary layer humidity fluxes and statistics from airborne DIAL. *J. Geophys. Res.*, 102 (D24), 29
3 189–29 204, doi: 10.1029/97JD01112, 1997.

4 Kiemle, C., Brewer, W. A., Ehret, G., Hardesty, R. M., Fix A., Senff, C., Wirth, M., Poberaj G., LeMone,
5 M. A.: Latent heat flux profiles from collocated airborne water vapour and wind lidars during
6 IHOP_2002. *J. Atm. Ocean. Tech.*, 24, 627–639, DOI: <http://dx.doi.org/10.1175/JTECH1997.1>, 2007.

7 Lenschow, D. H., and Kristensen, L.: Uncorrelated noise in turbulence measurements. *J. Atm. Ocean.*
8 *Tech.*, 12, 68–81, DOI: [http://dx.doi.org/10.1175/1520-0426\(1985\)002<0068:UNITM>2.0.CO;2](http://dx.doi.org/10.1175/1520-0426(1985)002<0068:UNITM>2.0.CO;2), 1985.

9 Lenschow, D. H., Wulfmeyer, V., Senff, C., Measuring second-through fourth-order moments in noisy
10 data. *J. Atm. Ocean. Tech.*, 17, 1330–1347, doi:10.1175/1520-0426(2000)0172.0.CO;2, 2000.

11 Mahrt, L.: Boundary-layer moisture regimes. *Q. J. Roy. Meteorol. Soc.* 117:151–176,
12 DOI: 10.1002/qj.49711749708, 1991.

13 McNicholas, C., and Turner, D. D.: Characterizing the convective boundary layer turbulence with a
14 High Spectral Resolution Lidar, *J. Geophys. Res. Atmos.*, 119, 12,910–12,927,
15 doi:10.1002/2014JD021867, 2014.

16 Milovac, J., Warrach-Sagi, K., Behrendt, A., Späth, F., Ingwersen, J., and Wulfmeyer, V.: Investigation
17 of PBL schemes combining the WRF model simulations with scanning water vapour differential
18 absorption lidar measurements. *J. Geophys. Res. Atmos.* 121 (2), 624–649,
19 DOI :10.1002/2015JD023927, 2016.

20 [Milroy, C., Martucci, G., Lolli, S., Loaec, S., Sauvage, L., Xueref-Remy, I., Lavrič, J. V., Ciais, P.,
21 Feist, D. G., Biavati, G., O'Dowd, C. D.: An Assessment of Pseudo-Operational Ground-Based Light
22 Detection and Ranging Sensors to Determine the Boundary-Layer Structure in the Coastal Atmosphere,
23 *Advances in Meteorology*, 2012, 18 pages, doi:10.1155/2012/929080, 2012.](#)

24 Muppa, S.K., Behrendt, A., Späth, F., Wulfmeyer, V., Metzendorf, S., and Riede, A.: Turbulent
25 humidity fluctuations in the convective boundary layer: Case studies using water vapour differential
26 absorption lidar measurements, *Bound.-Lay. Meteorol.*, 58 (1), 43-66. DOI:10.1007/s10546-015-0078-
27 9, 2016.

28 Newsom, R. K, Turner, D. D., Mielke, B., Clayton, M., Ferrare, R., Sivaraman, C.: The use of
29 simultaneous analog and photon counting detection for Raman lidar. *Appl. Opt.*, 48, 3903–3914,
30 doi: 10.1364/AO.48.003903, 2009.

1 Nocera, R., Raman lidar measurements of the atmospheric temperature vertical profile, Master Thesis,
2 Potenza, 2016.

3 Pal, S., Behrendt, A. and Wulfmeyer, V.: Elastic-backscatter lidar based characteri-zation of the
4 convective boundary layer and investigation of related statistics, *Ann. Geophys.* 28, 825-847,
5 DOI:10.5194/angeo-28-825-2010, 2010.

6 Radlach, M., Behrendt, A., and Wulfmeyer, V.: Scanning rotational Raman lidar at 355 nm for the
7 measurement of tropospheric temperature fields, *Atmos. Chem. Phys.*, 8, 159–169, doi:10.5194/acp-8-
8 159-2008, 2008.

9 Senff, C., Bösenberg, J., Peters, G., Schaberl, T.: Remote sensing of turbulent ozone fluxes and the
10 ozone budget in the convective boundary layer with DIAL and radar-RASS: a case study, *Contrib.*
11 *Atmos. Phys.*, 69, 161–176, 1996.

12 Sorbjan, Z.: Effects caused by varying the strength of the capping inversion based on a large eddy
13 simulation model of the shear-free convective boundary layer. *J Atmos Sci.*, 53, 2015-2024, 1996.

14 Späth, F., Metzendorf, S., Behrendt, A., Wizemann, H. D., Wagner, G., and Wulfmeyer, V.:
15 Online/offline injection seeding system with high frequency-stability and low crosstalk for water vapor
16 DIAL, *Opt. Commun.*, 309, 37–43, doi:10.1016/j.optcom.2013.07.003, 2013.

17 Späth, F., A. Behrendt, S. K. Muppa, S. Metzendorf, A. Riede, and V. Wulfmeyer: 3D water vapor field
18 in the atmospheric boundary layer observed with scanning differential absorption lidar. *Atmos. Meas.*
19 *Tech.*, 9, 1701-1720, doi:10.5194/amt-9-1701-2016, 2016.

20 Stull, R. B.: *An Introduction to Boundary Layer Meteorology*, Atmospheric Sciences Library, 1988.

21 Su, J., McCormick, M. P., Wu, Y., Lee III, R. B., Lei, L., Liu, Z., and Leavor, K. R.: Cloud temperature
22 measurement using rotational Raman lidar, *J. Quant. Spectrosc. Ra.*, 125, 45–50, 2013.

23 Sullivan P.P., Moeng C-H., Stevens B., Lenschow D.H., Mayor S.D.: Structure of the entrainment zone
24 capping the convective atmospheric boundary layer. *J Atmos Sci.*, 55, 3042–3064, 1998.

25 Summa, D., Di Girolamo, P., Stelitano, D., Cacciani, M.: Characterization of the planetary boundary
26 layer height and structure by Raman Lidar: Comparison of different approaches, *Atmos. Meas. Tech.*, 6,
27 3515-3525, doi: 10.5194/amt-6-3515-2013, 2013.

28 Turner, D.D., Wulfmeyer, V., Berg, L.K., and Schween, J.H.: Water vapor turbulence profiles in
29 stationary continental convective mixed layers, *J. Geophys. Res.* 119, 11,151-11,165,
30 DOI:10.1002/2014JD022202, 2014a.

1 Turner, D. D., Ferrare, R. A., Wulfmeyer, V., and Scarino, A. J.: Aircraft evaluation of ground-based
2 Raman lidar water vapor turbulence profiles in convective mixed layers. *J. Atmos. Oceanic Technol.*, 31,
3 1078–1088, doi:10.1175/JTECH-D-13-00075.1, 2014b.

4 Wagner, G., V. Wulfmeyer, F. Späth, A. Behrendt, and M. Schiller: Performance and specifications of a
5 pulsed high-power single-frequency Ti:Sapphire laser for water-vapor differential absorption lidar. *Appl.*
6 *Opt.* 52, 2454-2469, doi: 10.1364/AO.52.002454, 2013.

7 Whiteman, D. N.: Examination of the traditional Raman lidar technique. I. Evaluating the temperature-
8 dependent lidar equations, *Appl. Opt.*, 42, 2571-2592, doi: 10.1364/AO.42.002571, 2003.

9 Wulfmeyer, V.: Investigation of turbulent processes in the lower troposphere with water-vapour DIAL
10 and radar-RASS. *J. Atmos. Sci.*, 56, 1055–1076, doi: [http://dx.doi.org/10.1175/1520-](http://dx.doi.org/10.1175/1520-0469(1999)056<1055:IOTPIT>2.0.CO;2)
11 [0469\(1999\)056<1055:IOTPIT>2.0.CO;2](http://dx.doi.org/10.1175/1520-0469(1999)056<1055:IOTPIT>2.0.CO;2), 1999a.

12 Wulfmeyer, V.: Investigations of humidity skewness and variance profiles in the convective boundary
13 layer and comparison of the latter with large eddy simulation results. *J. Atmos. Sci.*, 56, 1077–1087,
14 doi: [http://dx.doi.org/10.1175/1520-0469\(1999\)056<1077:IOHSAV>2.0.CO;2](http://dx.doi.org/10.1175/1520-0469(1999)056<1077:IOHSAV>2.0.CO;2) ,1999b.

15 Wulfmeyer, V., *et al.*: [Research Campaign: the Convective and Orographically induced Precipitation](#)
16 [Study - RESEARCH CAMPAIGN: THE CONVECTIVE AND OROGRAPHICALLY INDUCED](#)
17 [PRECIPITATION STUDY](#) A Research and Development Project of the World Weather Research
18 Program for Improving Quantitative Precipitation Forecasting in Low-Mountain Regions. *Bulletin of*
19 *the American Meteorological Society*, 89, 1477-1486, ISSN: 0003-0007, doi:
20 [10.1175/2008BAMS2367.1](http://dx.doi.org/10.1175/2008BAMS2367.1), 2008.

21 Wulfmeyer, V., Turner, D. D., Pal, S., and Wagner, E.: Can water vapour Raman lidar resolve profiles
22 of turbulent variables in the convective boundary layer?, *Bound.-Lay. Meteorol.*, 136, 253-284,
23 doi:10.1007/s10546-010-9494-z, 2010.

24 Wulfmeyer, V., Hardesty, M., Turner, D.D., Behrendt, A., Cadeddu, M., Di Girolamo, P., Schlüssel, P.,
25 van Baelen, J., and Zus, F.: A review of the remote sensing of lower-tropospheric thermodynamic
26 profiles and its indispensable role for the understanding and the simulation of water and energy cycles,
27 *Rev. Geophys.*, 53, 819–895, DOI:10.1002/2014RG000476, 2015.

28 Wulfmeyer, V., Muppa, S., Behrendt, A., Hammann, E., Späth, F., Sorbjan, Z., Turner, D.D., and
29 Hardesty, R.M.: Determination of convective boundary layer entrainment fluxes, dissipation rates, and
30 the molecular destruction of variances: Theoretical description and a strategy for its confirmation with a
31 novel lidar system synergy, *J. Atmos. Sci.*, 73 (2), 667-692, doi: 10.1175/JAS-D-14-0392.1, 2016.

1 | [Wulfmeyer, W., and Turner, D. D.: Land-Atmosphere Feedback Experiment \(LAFE\) Science Plan,](#)
2 | [DOE/SC-ARM-16-038, www.arm.gov/publications/programdocs/doe-sc-arm-16-038.pdf, 2016.](#)
3

1 **Figures captions**

2 **Figure 1:** Profiles of noise error affecting water vapour mixing ratio (panels a and b) and temperature
3 (panel c) measurements. The figure illustrates the estimates determined based on the application of the
4 auto-covariance method, obtained by extrapolating the structure function to lag zero, and the error
5 profiles obtained based on the application of Poisson statistics to signal photon counts.

6 Time-height cross-section of the particle backscatter coefficient, β_{par} , between 11:30 and 13:30 UTC on
7 20 April 2013. The black line in the figure identifies the CBL height z_i .

8 **Figure 2:** (panel a) The mean photon numbers (10 sec average) for the considered signals, i.e. the water
9 vapour and molecular nitrogen vibrational Raman signals, $P_{H_2O}(z)$ and $P_{N_2}(z)$, the 355 nm elastic
10 signal, $P_{355}(z)$, and the pure-rotational Raman signals, $P_{LoJ}(z)$ and $P_{HiJ}(z)$; (panel b) temperature
11 sensitivity of RRL measurement technique. $\partial R(z)/\partial T$.

12 **Figure 3:** Vertical profiles of $P_{LoJ}^{leak}(z)$, $P_{HiJ}(z)$, $T_F P_{354.7}(z)$ and $P_{LoJ}^{synt}(z)$ for the time interval 13:38-13:46
13 UTC on 20 April 2013, revealing the presence of high cirrus clouds extending between 7.9 and 9.8 km.

14 **Figure 4:** Time-height cross-section of the particle backscatter coefficient, β_{par} , between 11:30 and
15 13:30 UTC on 20 April 2013. The black line in the figure identifies the CBL height z_i .

16 **Figure 5:** Time-height cross section of water vapour mixing ratio (panel a) and temperature (panel b) in
17 the same time interval considered in figure 4.

18 **Figure 6:** Mean water vapour mixing ratio (panel a) and temperature (panel b) profiles measured by
19 *BASIL* on 20 April 2013 between 11:30 and 13:30 UTC, together with the corresponding profiles as
20 measured by a radiosonde launched at 13:00 UTC from the nearby site of Hambach. Noise error bars
21 are also shown.

22 **Figure 7:** Time-height cross section of water vapour mixing ratio (panel a) and temperature fluctuations
23 (panel b) in the same time interval considered in figure 4.

24 **Figure 8:** Auto-covariance functions obtained from the measured water vapour mixing ratio (panel a)
25 and temperature (panel b) fluctuations in the same time interval considered in figure 4. Auto-covariance
26 functions are displayed for the height levels between 400 and 1600 m a.g.l., i.e., 0.3 to 1.25 z_i , for lags
27 from -200 to 200 s.

28 **Figure 9:** Integral scale of water vapour mixing ratio (panel a) and temperature fluctuations (panel b)
29 computed for the same time interval considered in figure 4.

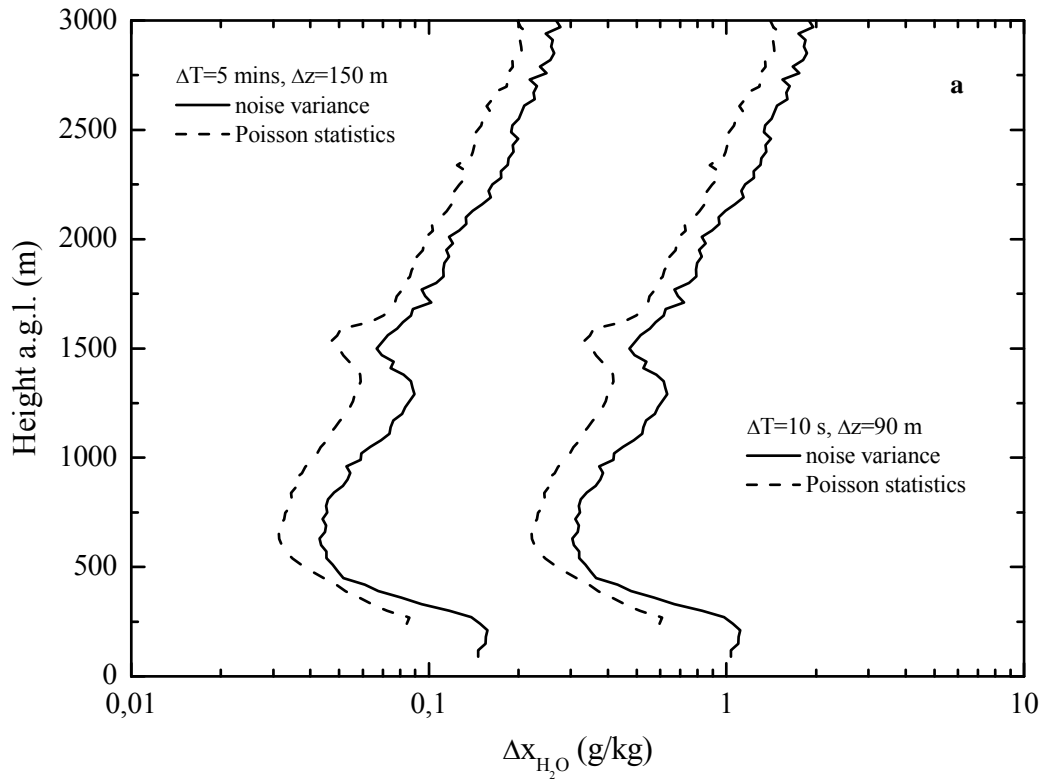
1 **Figure 10:** Vertical profiles of atmospheric and total variance for water vapour mixing ratio (panel a)
2 and temperature (panel b) computed for the same time interval considered in figure 4. In the figure the
3 error bars represent only the noise error.

4 **Figure 11:** Vertical profiles of the third-order moment for water vapour mixing ratio (panel a) and
5 temperature (panel b) computed for the same time interval considered in figure 4. In the figure the error
6 bars represent only the noise error.

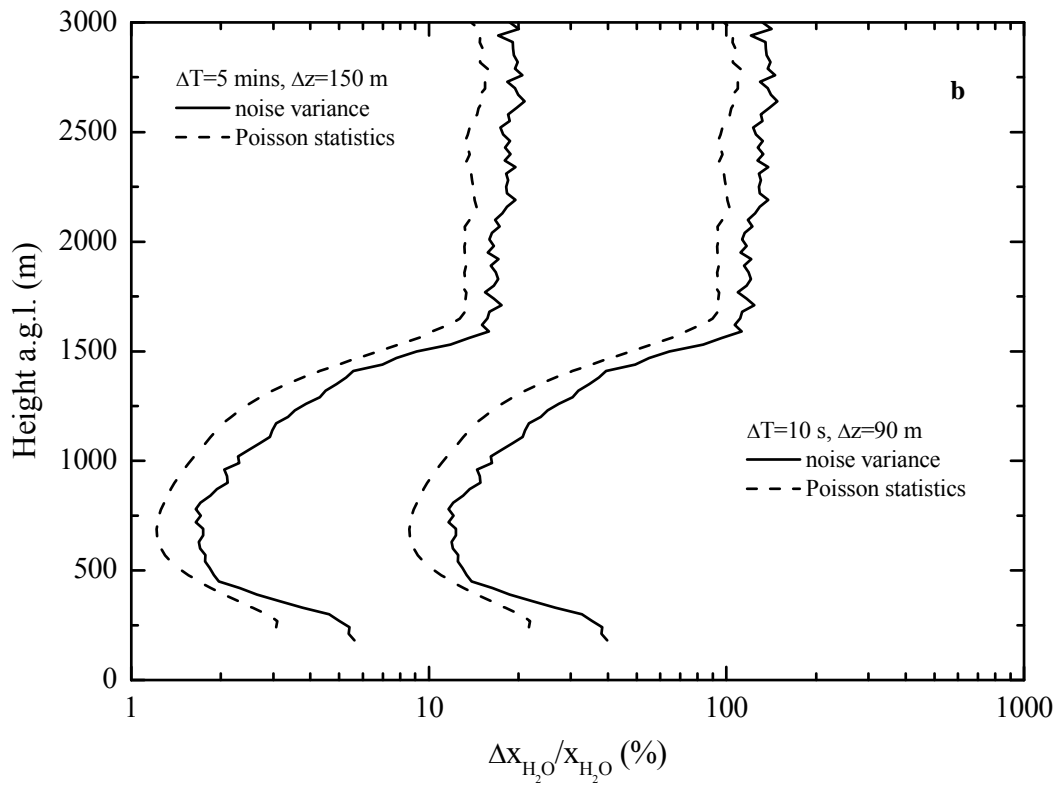
7 **Figure 12:** Vertical profiles of the fourth-order moment for water vapour mixing ratio (panel a) and
8 temperature (panel b) computed for the same time interval considered in figure 4. In the figure the error
9 bars represent only the noise error.

10 **Figure 13:** Vertical profiles of skewness (panel a) and kurtosis (panel b) for water vapour mixing ratio
11 and temperature computed for the same time interval considered in figure 4. In the figure the thick error
12 bars represent the noise error, while the thin error bars represent the sampling error.

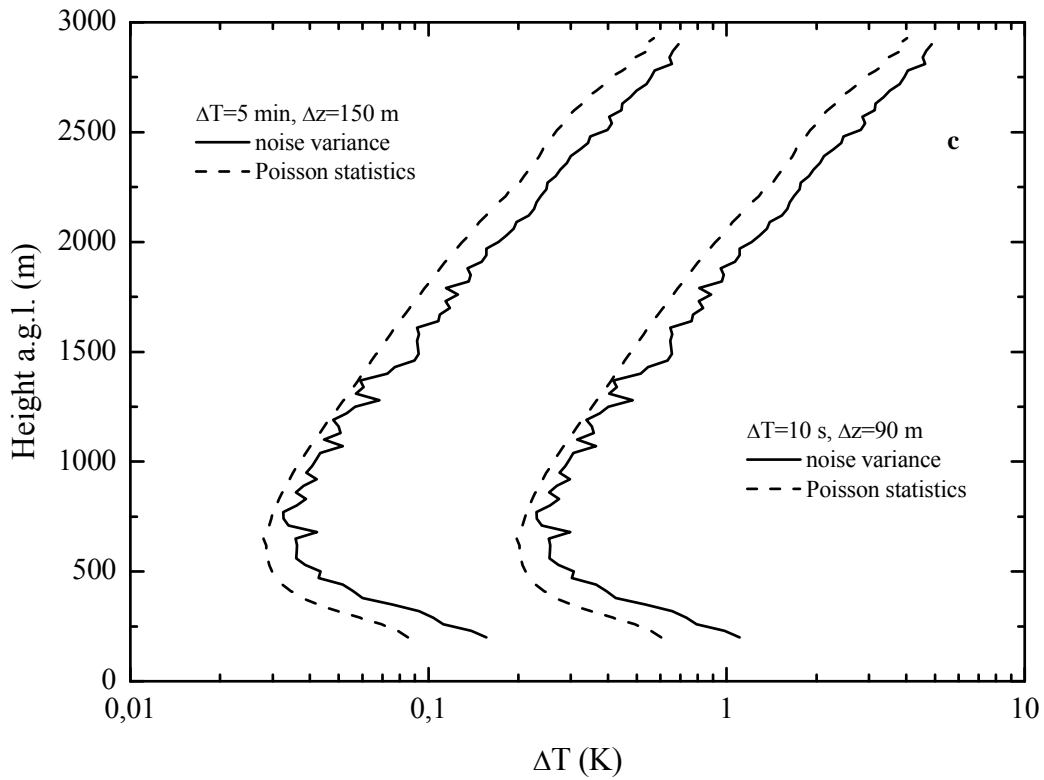
13



1



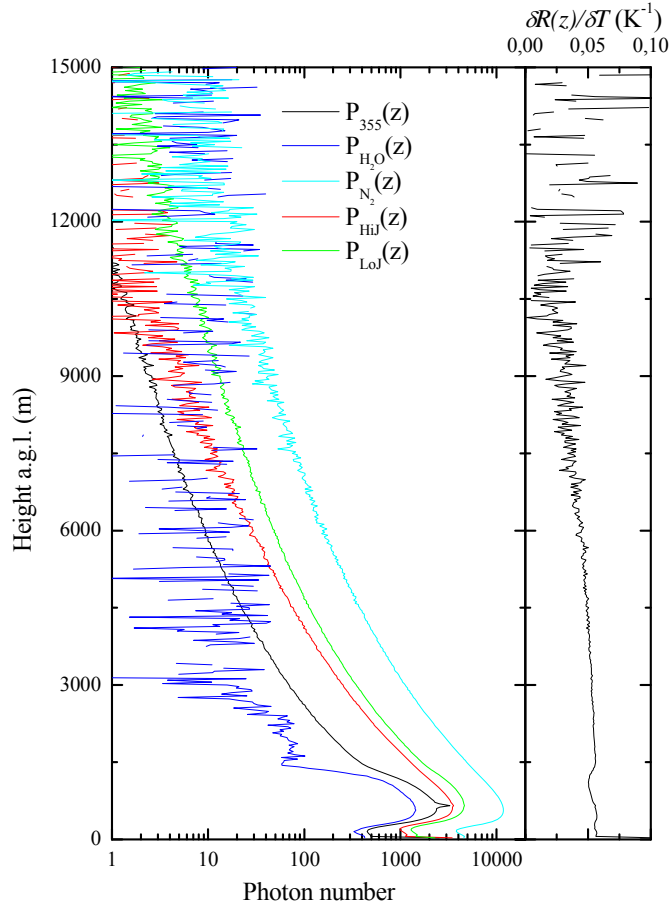
2



1

2 **Figure 1:** Profiles of noise error affecting water vapour mixing ratio (panels a and b) and temperature
 3 (panel c) measurements. The figure illustrates the estimates determined based on the application of the
 4 auto-covariance method, obtained by extrapolating the structure function to lag zero, and the error
 5 profiles obtained based on the application of Poisson statistics to signal photon counts.

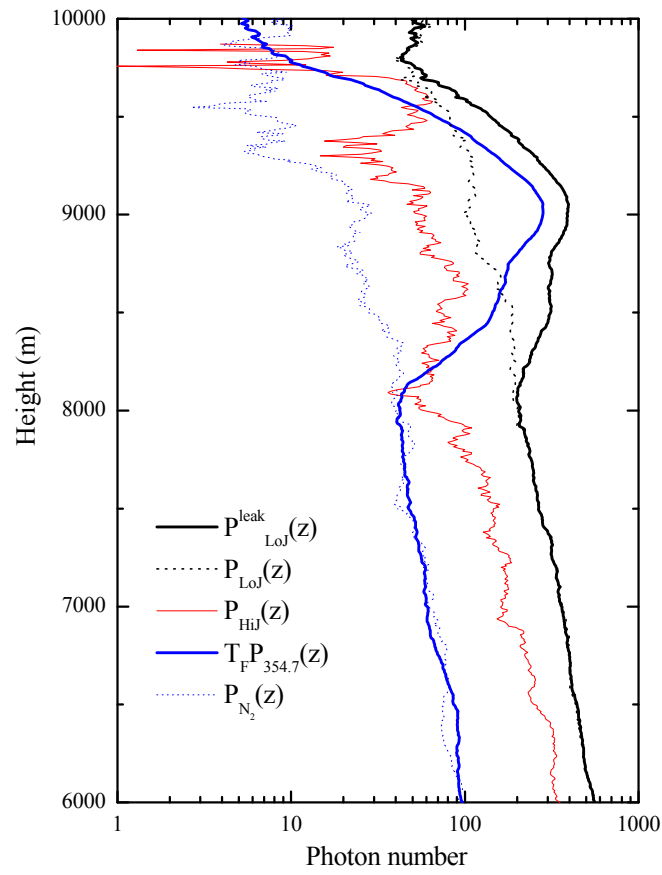
6



1

2 **Figure 2:** (panel a) The mean photon numbers (10 sec average) for the considered signals, i.e. the water
 3 vapour and molecular nitrogen vibrational Raman signals, $P_{H_2O}(z)$ and $P_{N_2}(z)$, the 355 nm elastic
 4 signal, $P_{355}(z)$, and the pure-rotational Raman signals, $P_{LoJ}(z)$ and $P_{HiJ}(z)$; (panel b) temperature
 5 sensitivity of RRL measurement technique. $\partial R(z)/\partial T$.

6

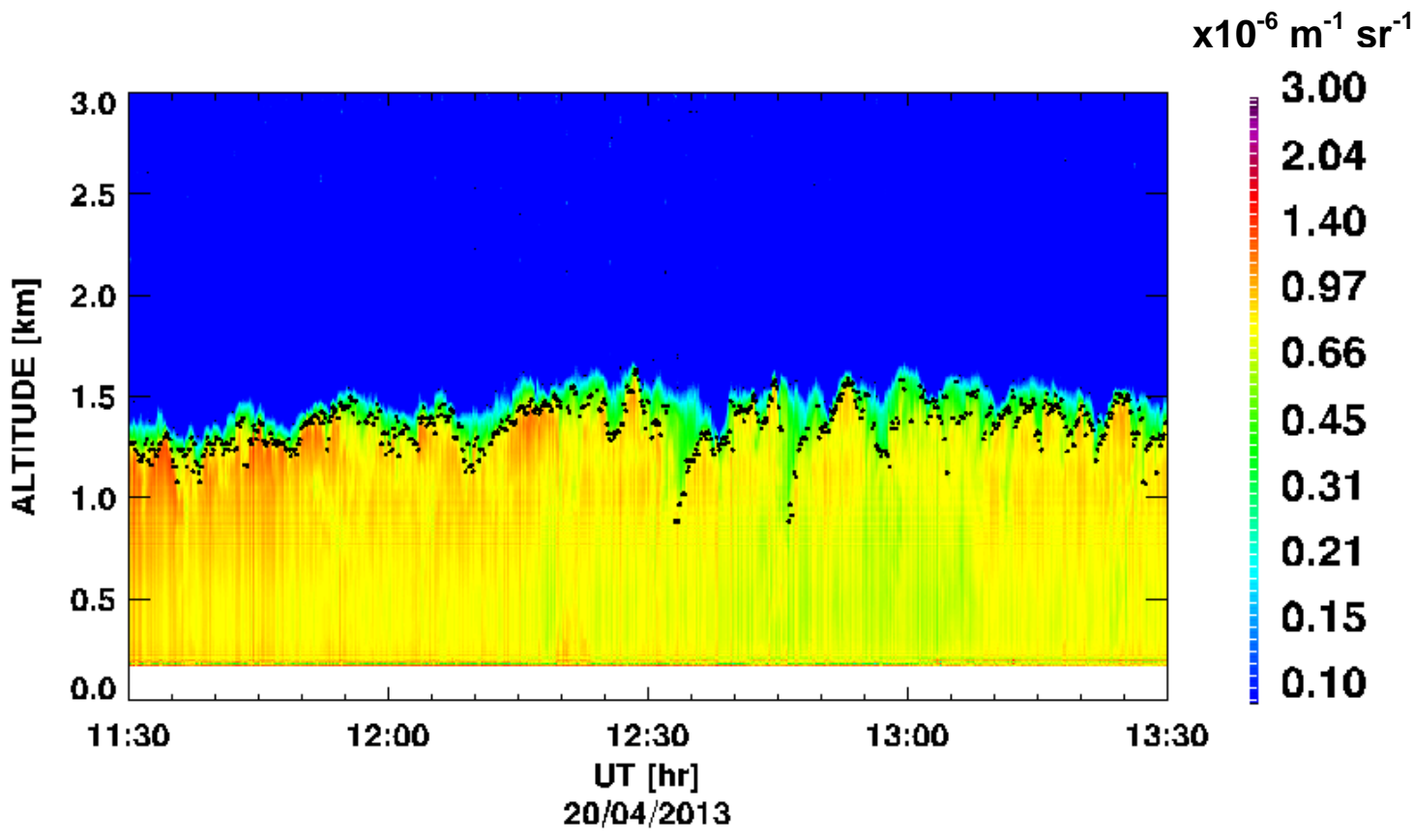


1

2 **Figure 3:** Vertical profiles of $P_{LoJ}^{leak}(z)$, $P_{HiJ}(z)$, $T_F P_{354.7}(z)$ and $P_{LoJ}^{synth}(z)$ for the time interval 13:38-13:46
 3 UTC on 20 April 2013, revealing the presence of high cirrus clouds extending between 7.9 and 9.8 km.

4

1

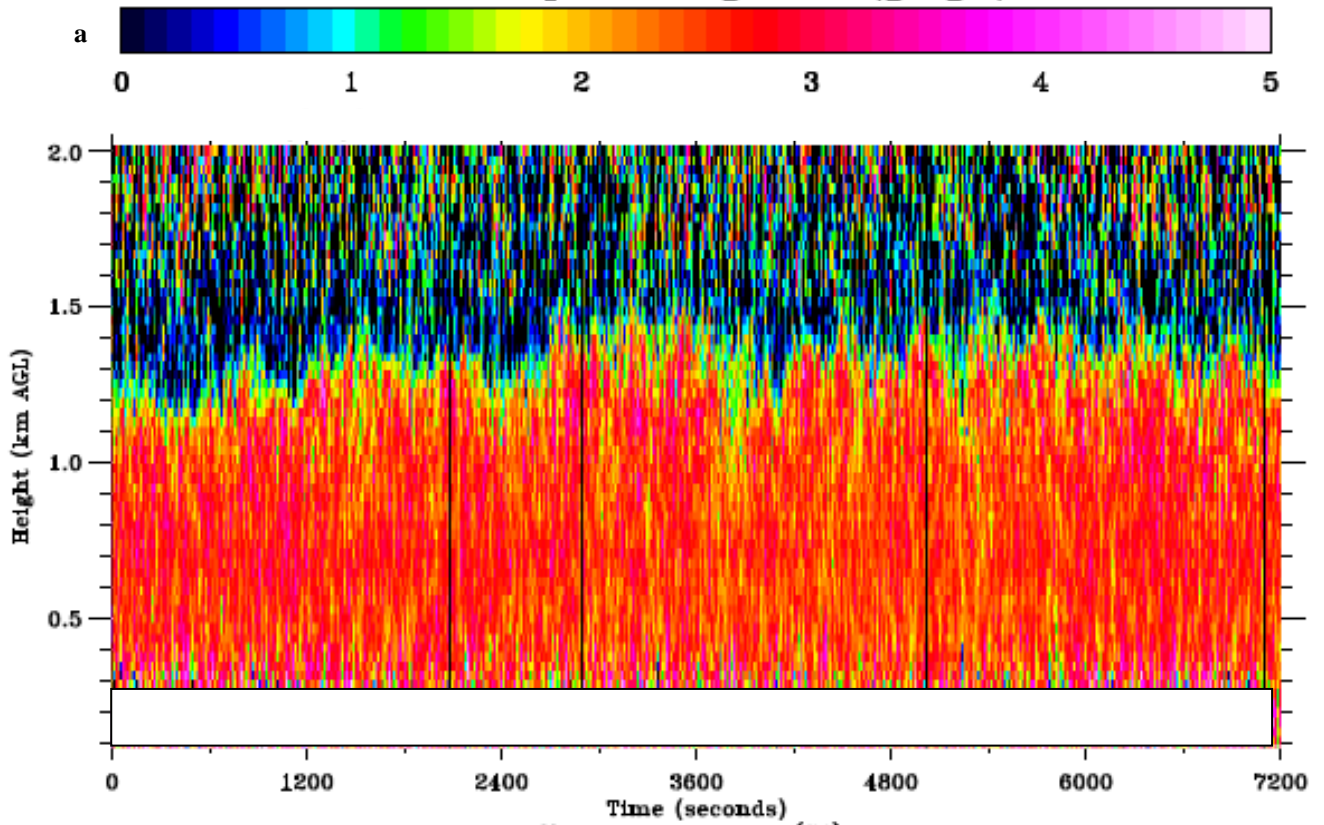


2

3 **Figure 4:** Time-height cross-section of the particle backscatter coefficient, β_{par} , between 11:30 and
4 13:30 UTC on 20 April 2013. The black line in the figure identifies the CBL height z_i .

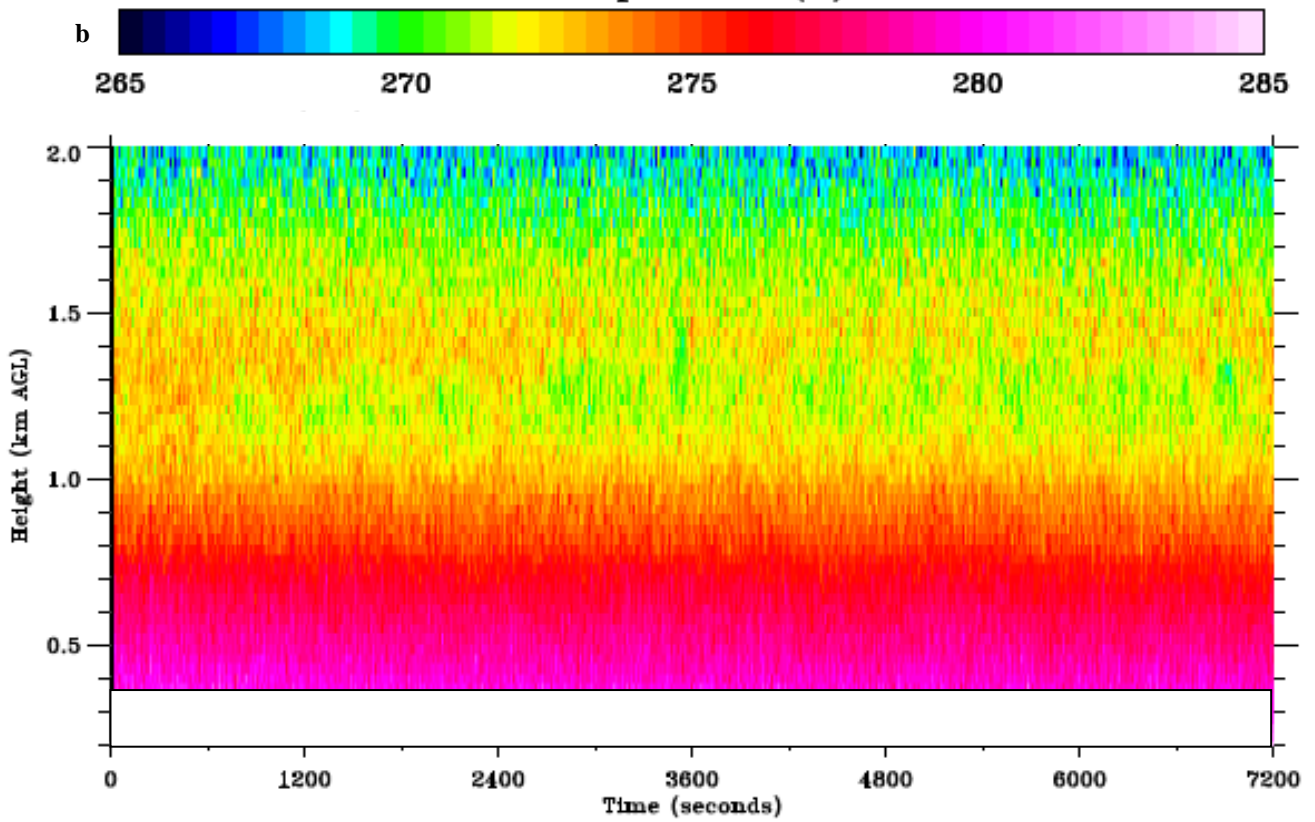
5

Water Vapor Mixing Ratio (g kg^{-1})



1

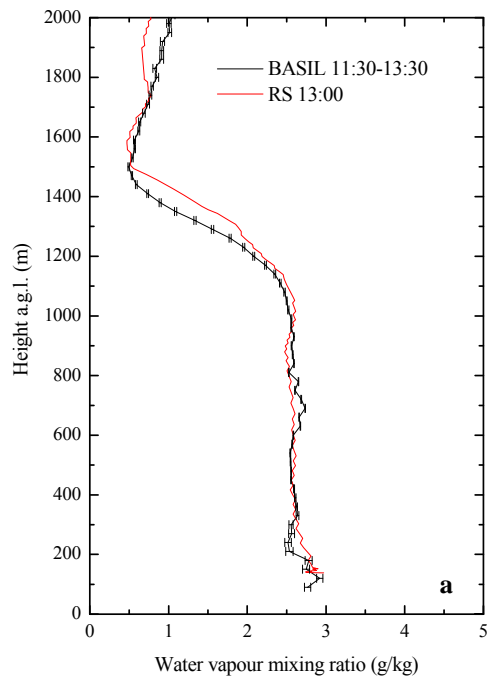
Temperature (K)



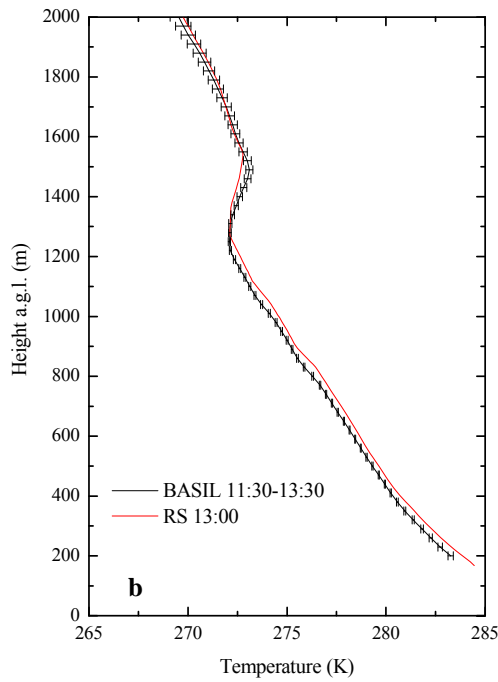
2

3 **Figure 5:** Time-height cross section of water vapour mixing ratio (panel a) and temperature (panel b) in
4 the same time interval considered in figure 4.

1



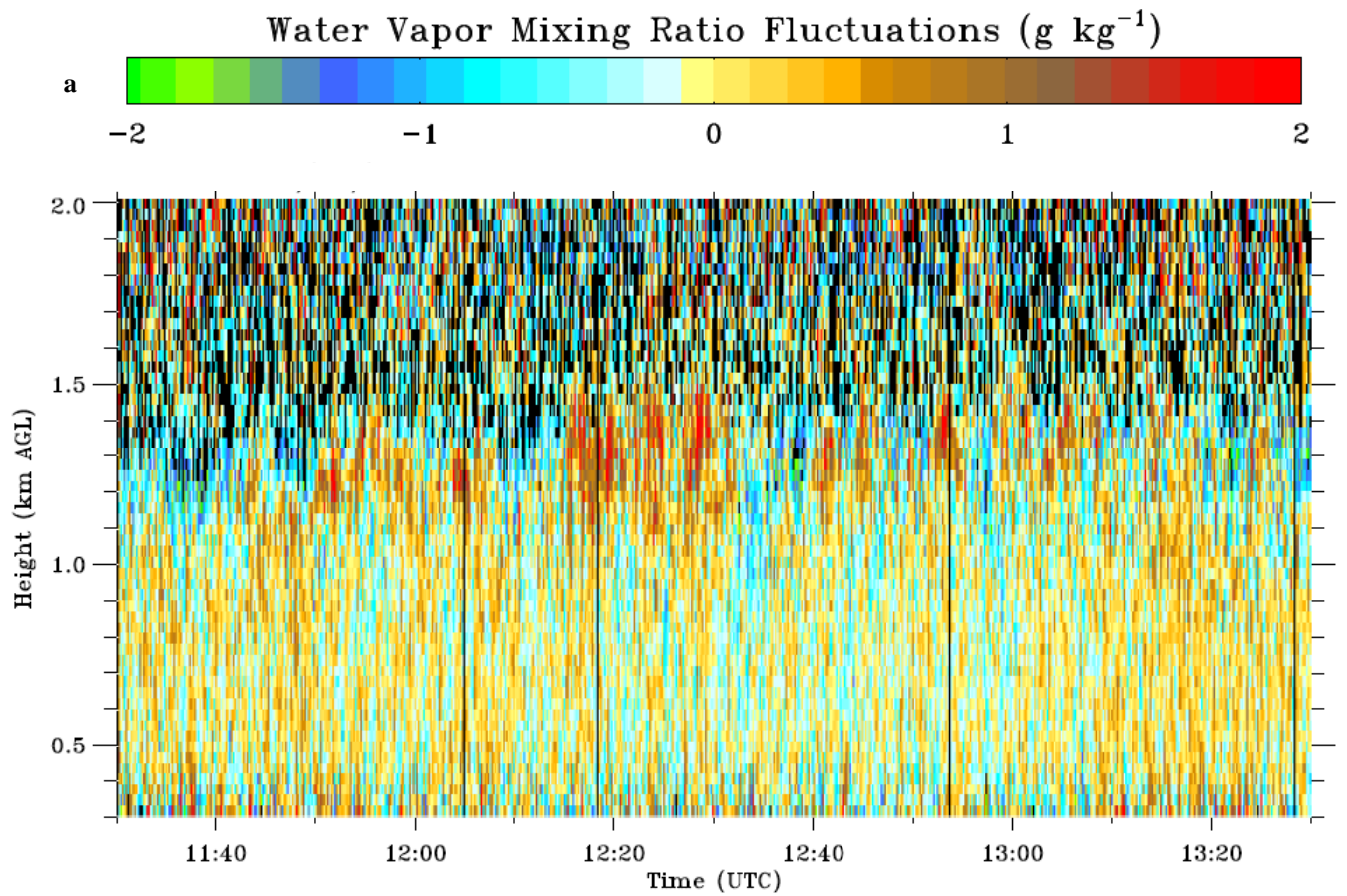
2



3

4 **Figure 6:** Mean water vapour mixing ratio (panel a) and temperature (panel b) profiles measured by
5 *BASIL* on 20 April 2013 between 11:30 and 13:30 UTC, together with the corresponding profiles as
6 measured by a radiosonde launched at 13:00 UTC from the nearby site of Hambach. Noise error bars
7 are also shown.

1



2
3
4
5

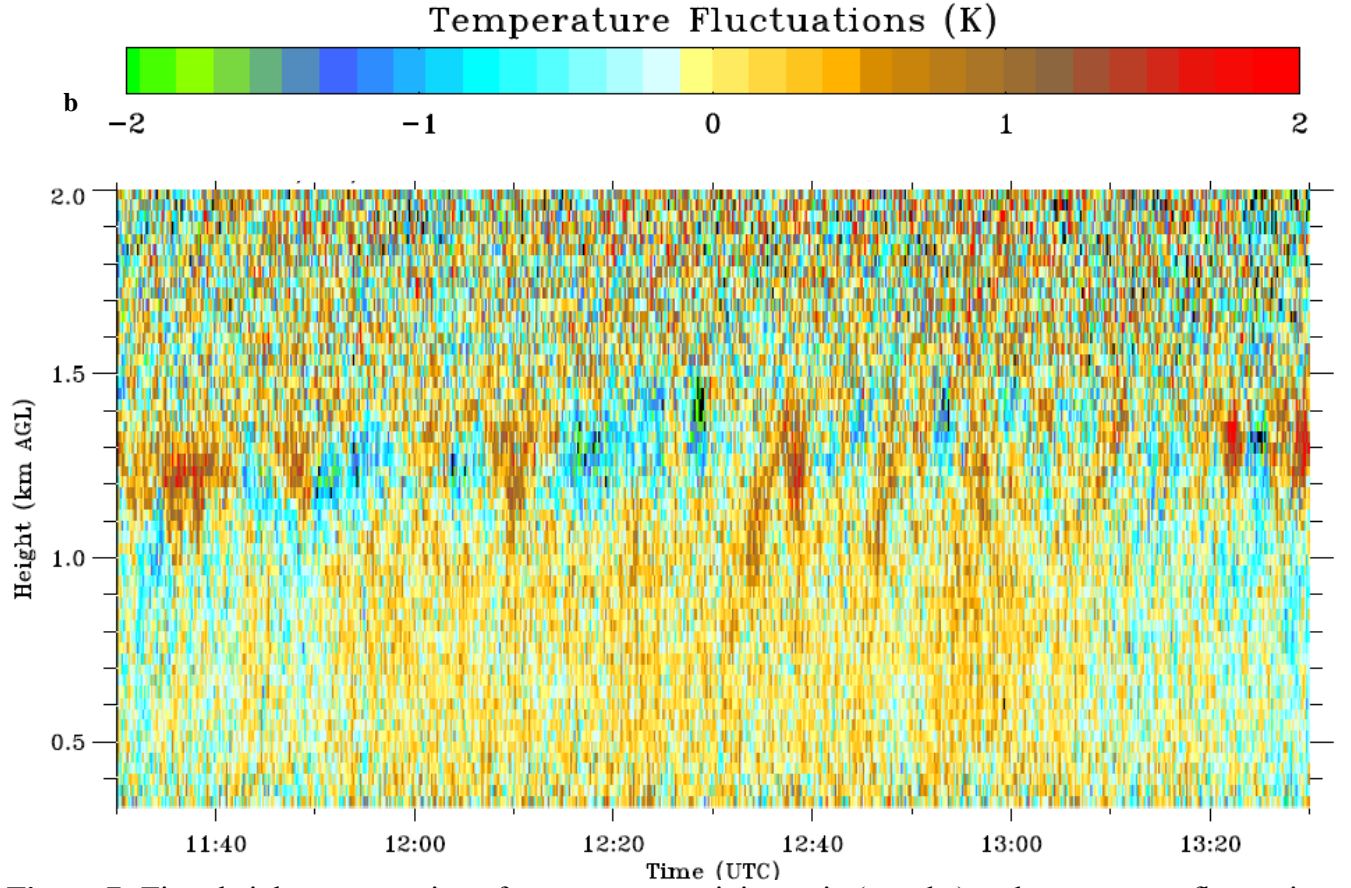
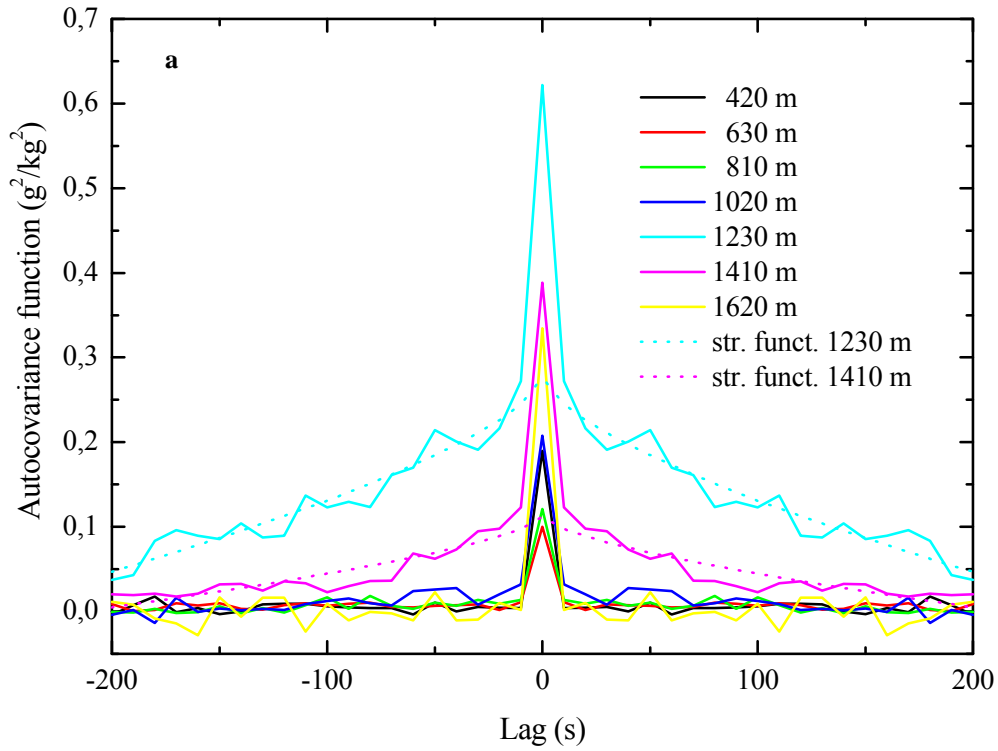
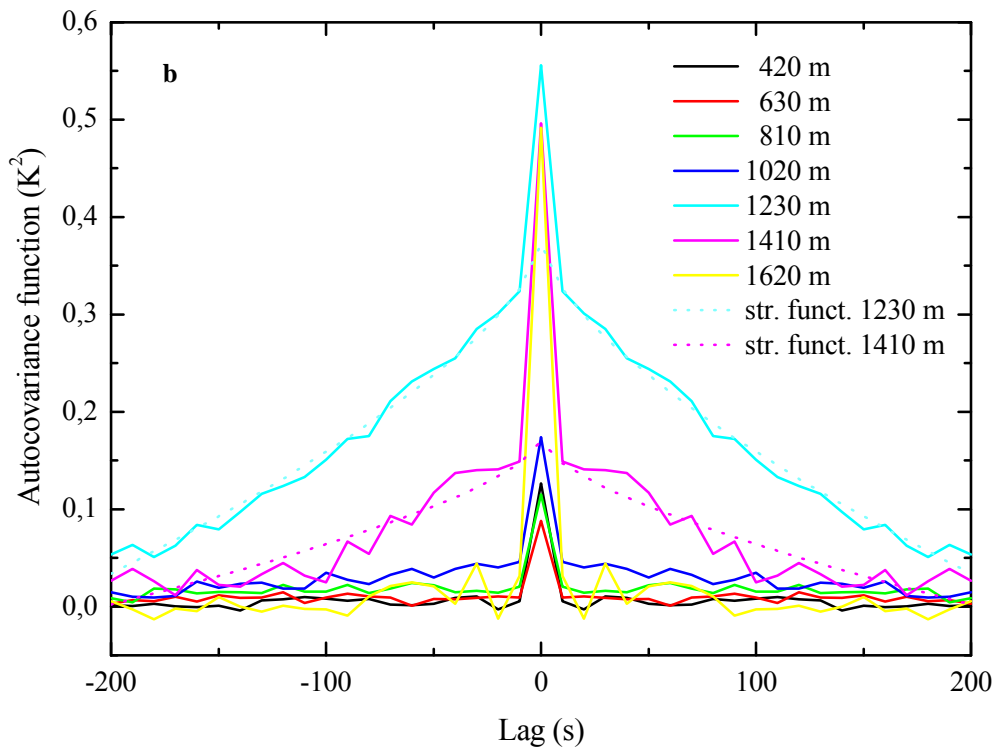


Figure 7: Time-height cross section of water vapour mixing ratio (panel a) and temperature fluctuations (panel b) in the same time interval considered in figure 4.



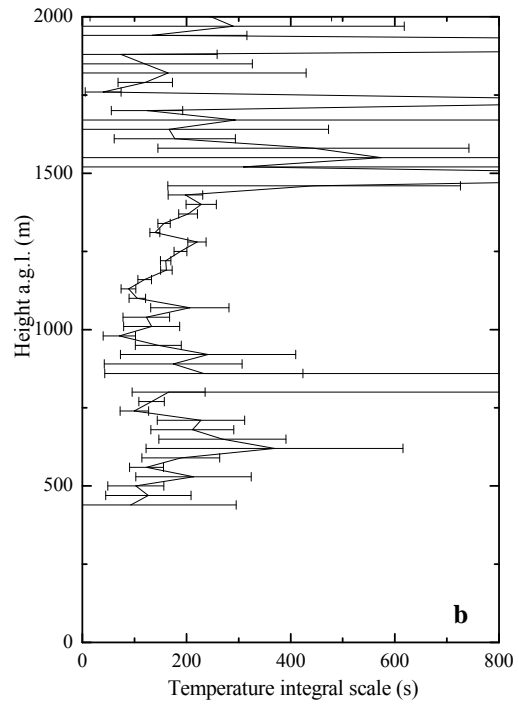
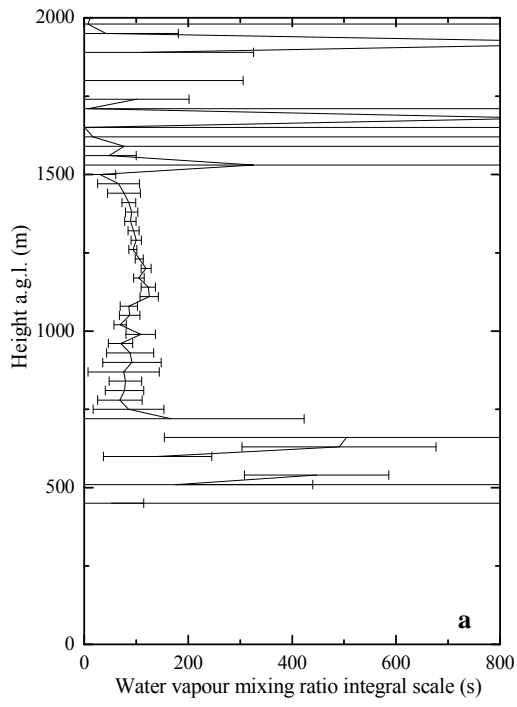
1



2

3 **Figure 8:** Auto-covariance functions obtained from the measured water vapour mixing ratio (panel a)
 4 and temperature (panel b) fluctuations in the same time interval considered in figure 4. Auto-covariance
 5 functions are displayed for the height levels between 400 and 1600 m a.g.l., i.e., 0.3 to 1.25 z_i , for lags
 6 from -200 to 200 s.

7

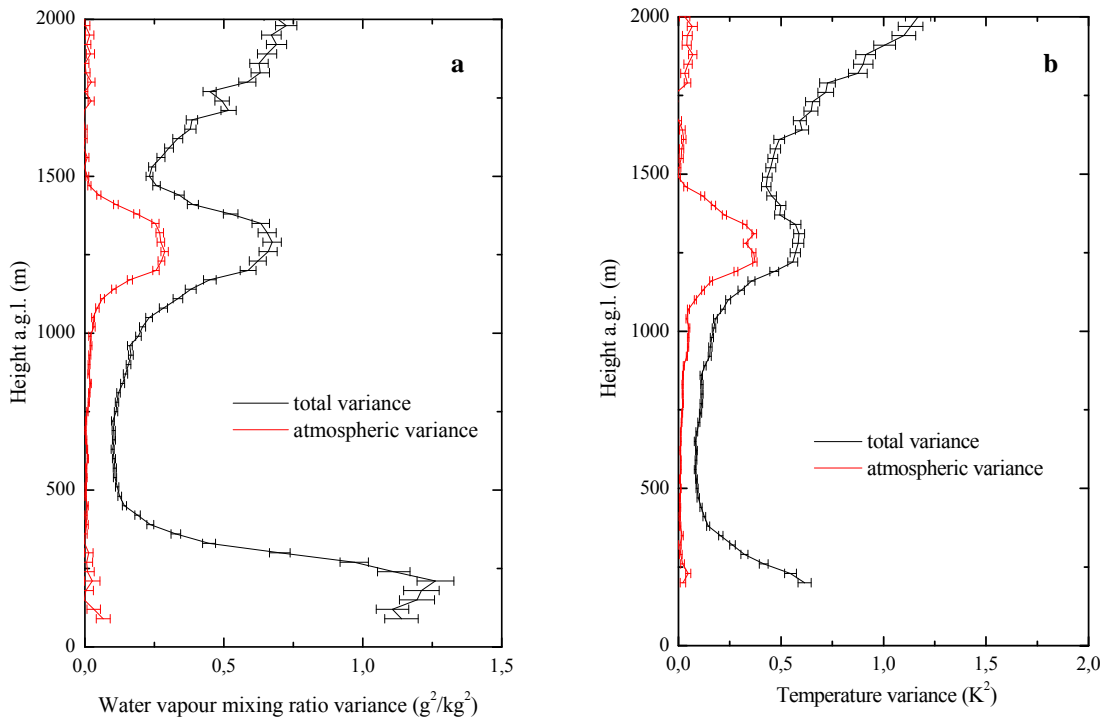


1

2 **Figure 9:** Integral scale of water vapour mixing ratio (panel a) and temperature fluctuations (panel b)
3 computed for the same time interval considered in figure 4.

4

1

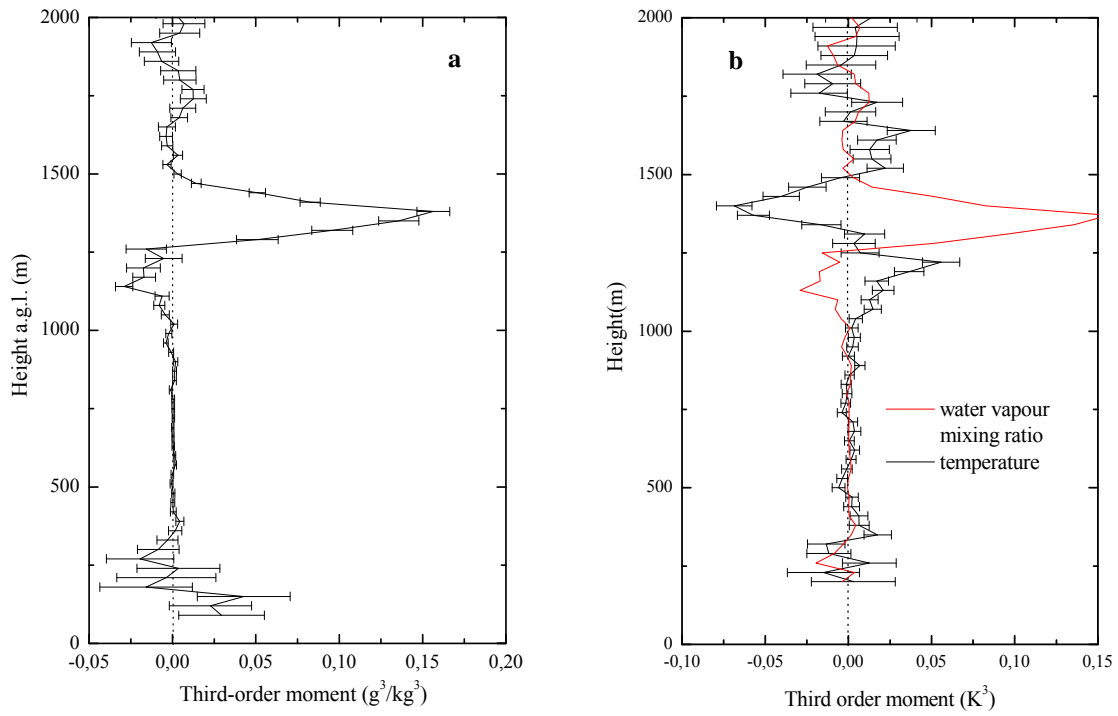


2

3 **Figure 10:** Vertical profiles of atmospheric and total variance for water vapour mixing ratio (panel a)
4 and temperature (panel b) computed for the same time interval considered in figure 4. In the figure the
5 error bars represent only the noise error.

6

7

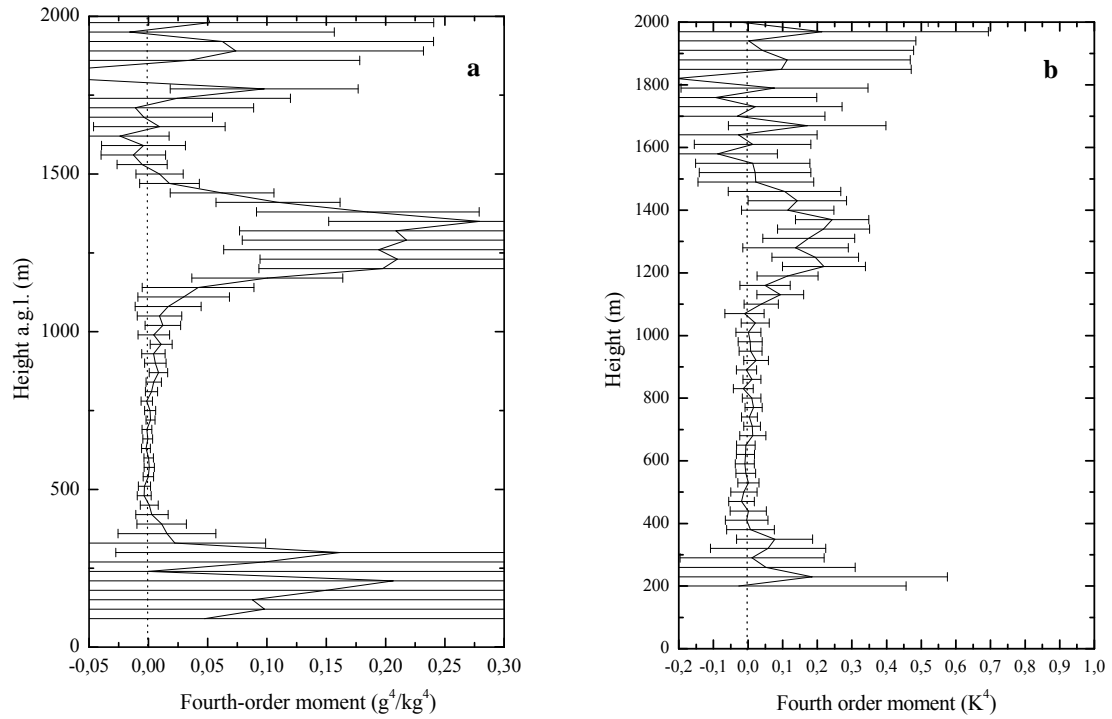


1

2 **Figure 11:** Vertical profiles of the third-order moment for water vapour mixing ratio (panel a) and
 3 temperature (panel b) computed for the same time interval considered in figure 4. In the figure the error
 4 bars represent only the noise error.

5

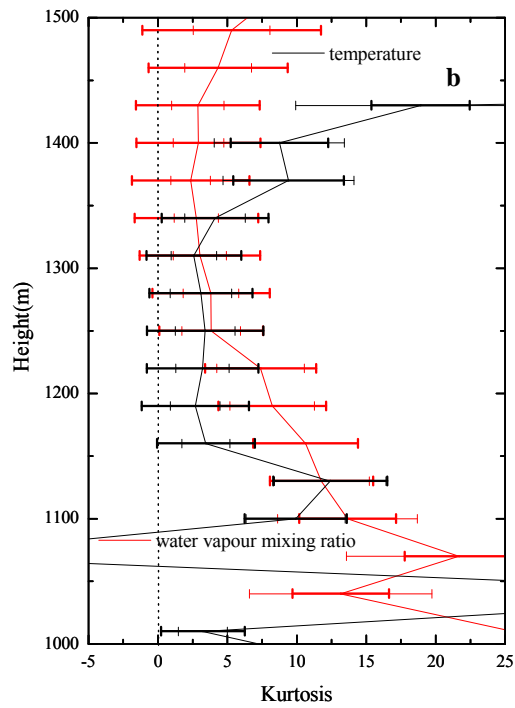
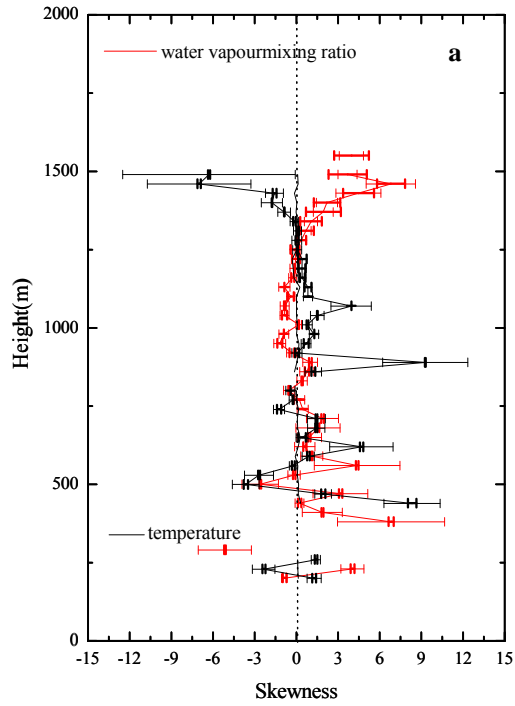
1



2

3 **Figure 12:** Vertical profiles of the fourth-order moment for water vapour mixing ratio (panel a) and
4 temperature (panel b) computed for the same time interval considered in figure 4. In the figure the error
5 bars represent only the noise error.

6



1
2
3
4
5
6
7
8
9
10
11
12
13
14
15
16
17
18
19
20
21
22
23

Figure 13: Vertical profiles of skewness (panel a) and kurtosis (panel b) for water vapour mixing ratio and temperature computed for the same time interval considered in figure 4. In the figure the thick error bars represent the noise error, while the thin error bars represent the sampling error.